applied system innovation

MDPI

Article

Adaptive Reactive-Power-Priority Fuzzy Q + P Voltage Control in PV-Rich Low-Voltage Distribution Networks: A Multi-Criteria Scenario-Based Comparison with Q(U) Control

Daiva Stanelytė [1,2,*] and Virginijus Radziukynas [2]

[1] Transport, Electrical and Mechanical Engineering Department, Klaipėdos Valstybinė Kolegija/Higher Education Institute, LT-91274 Klaipeda, Lithuania
[2] Smart Grids and Renewable Energy Laboratory, Lithuanian Energy Institute (LEI), LT-44403 Kaunas, Lithuania; virginijus.radziukynas@lei.lt
* Correspondence: d.stanelyte@gmail.com; Tel.: +370-605-35435

Abstract

Smart-inverter Volt–Var and Volt–Watt control is established practice, but the relative merits of local controller architectures depend on network conditions and inverter capability. This simulation-based study evaluates a reactive-power-priority adaptive Fuzzy Q + P controller against fixed Q(U), conventional Q(U) + P(U), and Q(U) with the same selective P(U) decision mechanism, together with the Fuzzy Q-only and uncontrolled cases. All six cases were assessed under 400 matched 48 h scenarios using a balanced three-phase quasi-steady-state equivalent. Relative to Q(U), Fuzzy Q + P reduced exposure above 1.11 p.u. by 2.20% and modelled voltage-protection trips by 3.98%, with 48.33% greater reactive-power effort and 0.23% less generated PV energy. Against conventional Q(U) + P(U), the critical-overvoltage duration was 1.17% shorter, but trips were 1.59% more frequent, generated PV energy was 0.57% lower, and reactive-power effort was 46.89% higher. Direct P(U) curtailment occurred in 113 of the 400 scenarios. An uncalibrated equivalent feeder-voltage calculation was separately assessed against 81,951 synchronized real-site samples (RMSE 0.001038 p.u.); this does not experimentally validate the controllers. The time-step convergence assessment did not meet its predefined acceptance criteria; therefore, protection-related results should be interpreted as numerical indicators within the implemented model. The findings therefore indicate a scenario-dependent voltage-security–energy–reactive-effort trade-off, not universal superiority over established combined control.

Keywords: low-voltage distribution network; photovoltaic generation; voltage regulation; Volt–Var control; Q(U) control; fuzzy logic control; reactive power control; active power curtailment; smart inverter

Check for updates

Academic Editor: Igor Korobiichuk

Received: 20 September 2026
Revised: 12 October 2026
Accepted: 27 October 2026
Published: 30 October 2026

Copyright: © 2026 by the authors. Published by MDPI on behalf of the International Institute of Knowledge Innovation and Invention. Licensee MDPI, Basel, Switzerland. This article is an open access article distributed under the terms and conditions of the Creative Commons Attribution (CC BY) license.

1. Introduction

In the last two decades, the proportion of distributed renewable energy resources within electric power systems has risen markedly. With their adoption increasing, voltage and reactive-power control has become a key topic of research in distribution networks [1,2]. Operational conditions in distribution networks are continuously shifting because fluctuations in generation and load change power-flow distribution and voltage profiles [3]. Voltage deviations, covering both voltage drop and voltage rise, are among the key power-quality concerns in low-voltage distribution networks [4]. Variations in electrical load alongside the integration of distributed generation can alter the voltages at network nodes. As these

operating conditions shift, they may increase the likelihood that the system experiences violations of the allowable voltage limits, making such breaches occur more often than under more stable loading and generation conditions [5].

As DER penetration increases, power flow in distribution feeders can become bidirectional. During periods of high local PV generation and low demand, reverse active power flow can modify the local voltage profile and may contribute to voltage-rise conditions, with the severity depending on feeder characteristics, loading, DER location, and the available voltage-control functions. In contemporary distribution networks, such operating conditions are addressed through interconnection requirements and smart-inverter functions, including Volt–Var and Volt–Watt control, rather than being treated as an unmanaged consequence of reverse power flow [6].

These voltage-control sensitivities are particularly relevant in radial low-voltage distribution networks. In such systems, the resistive portion of the line impedance is frequently more prominent than in networks operating at higher voltage levels. Since, in the present study, the impedance composition is represented through the X/R ratio, a network with a greater degree of resistive behaviour is associated with a lower X/R value. As a result, the voltage at the point of interconnection responds not only to changes in the transfer of reactive power, but also to fluctuations in the transfer of active power. In practical terms, this means that alterations in distributed-generation output and in load demand can produce substantial voltage deviations [7–9]. The relevance of these phenomena becomes especially pronounced when distributed-generation output is high, when load conditions vary, and when the overall network is weak [10]. Accordingly, evaluations of the effectiveness of voltage control should be based on both the network strength and the impedance composition, rather than focusing on either aspect in isolation.

Smart-inverter-based voltage regulation is now an established component of modern DER integration. Contemporary interconnection frameworks provide autonomous voltage-support functions, including Volt–Var and Volt–Watt control, while increasingly visible and controllable DERs can also be coordinated through supervisory distribution-management platforms such as DERMS and ADMS. Consequently, the research question addressed here is not whether smart-inverter voltage-support functions are available, but how local control characteristics and adaptive decision rules should be designed and parameterized to balance voltage performance, reactive-power effort, and active power curtailment under varying operating conditions [6,9].

Among these local functions, Q(U) is one of the most widely used forms of autonomous Volt–Var control, where the inverter's reactive-power generation or absorption is determined by the local voltage at the point of connection. By doing so, the inverter can regulate reactive power autonomously based on the locally measured voltage, which means it does not need continuous communication with a central controller. Prior research has indicated that Q(U) control can effectively keep voltage within allowable limits and enhance the voltage profile [10,11]. However, the performance of local Volt–Var control is determined by the electrical properties of the network, particularly, short-circuit strength, the impedance X/R ratio, and how responsive the point-of-connection voltage is to variations in reactive power. In addition, the control capability is constrained by the reactive-power reserve available to the inverter at a given operating point. A limitation of the fixed Q(U) benchmark adopted in this study is that its voltage–reactive-power characteristic is not adapted across the investigated network and operating conditions. Consequently, its performance may vary across different network strengths, X/R ratios, and generation and load conditions. In the present study, Q(U) is deliberately implemented as a fixed piecewise-linear reference characteristic. This modelling choice should not be interpreted as implying that contemporary Volt–Var control is inherently non-adjustable. IEEE 1547-type Volt–Var rules can be parameterized

through their deadband, slopes, saturation levels, reference voltage, and response characteristics, and recent studies have investigated systematic optimization and customization of these parameters for different grid conditions. Accordingly, the fixed Q(U) controller used here represents a clearly defined piecewise-linear benchmark against which the proposed state- and network-conditioned fuzzy architecture is evaluated [12].

Beyond fixed local characteristics, adaptive, optimization-based, data-driven, and fuzzy-control approaches have been investigated to tailor inverter response to changing network and operating conditions [13]. The design and parameterization of local Volt–Var characteristics remain active research topics because control-curve parameters can affect not only steady-state voltage regulation but also closed-loop stability and convergence [12,14]. Fuzzy logic controllers (FLCs) do not necessitate a precise mathematical representation of the system to ascertain the control action. They are frequently used in voltage and reactive-power control issues because they are resilient to parameter changes and uncertainty [15–22]. Fuzzy control also has the advantage of a non-linear control response toward voltage changes, and the strength of control can be adapted to varying network operation conditions. In smart Volt-Var controllers, reactive-power control can be adapted to several variables that describe the network state and inverter operating condition, thus enabling the control response to be conditioned on multiple network-state and inverter operating variables [23]. Adaptive Volt-Var control that explicitly considers grid strength and PV inverter characteristics has also been reported [24]. Adaptive and fuzzy-logic-based approaches have been studied to improve the Volt–Var control performance by adapting the control action to the network state, thus reducing voltage deviations, and making a more efficient use of the available reactive-power reserve of the inverter [25].

Stanelytė and Narščius proposed a MATLAB/Simulink-based methodology to design and compare PID and Mamdani fuzzy Volt–Var controllers for a low-voltage feeder [17]. Although both studies use MATLAB-based implementations, the present work addresses a different control question and controller architecture. Specifically, it combines SCR/X/R-conditioned adaptive Fuzzy Q control with reactive-power headroom and overvoltage-warning information, one-step post-Q PCC voltage prediction, and selective P(U) activation. The proposed framework is evaluated using 400 matched scenarios, protection-state modelling, repeatability and sensitivity analyses, and separate real-site validation of the equivalent LV feeder-voltage calculation.

When reactive-power regulation alone is insufficient to maintain acceptable voltage conditions, Volt–Watt P(U) control can provide additional overvoltage mitigation by reducing active power injection [9,26]. This action introduces an explicit voltage–energy trade-off because stronger active power curtailment can improve voltage conditions while reducing the PV energy delivered to the grid [9]. Combined Volt–Var and Volt–Watt operation has already been investigated in the literature, including reactive-power-priority implementations in which reactive-power support is used first and active power curtailment is introduced when the available reactive-power capability is insufficient [26]. Accordingly, combined Volt–Var and Volt–Watt operation is treated here as established practice rather than as the novelty of the study. The present work instead focuses on the design and parameterization of a local adaptive control response under varying network and operating conditions. However, the dynamic performance of Volt–Var and Volt–Watt functions depends on their control settings, response time, network voltage sensitivity, and system conditions, which makes controller parameterization an important part of their practical implementation [12].

The recent literature shows that Volt–Var and Volt–Watt functions, coordinated DER control, and the design and optimization of local inverter-control rules are already established research areas [9,12]. Studies have addressed optimal Volt–Var curve design, combined Volt–Var/Volt–Watt operation, stability-oriented control setting selection, and

active power curtailment strategies under varying network conditions [12,13,27]. The gap addressed here is therefore narrower: it concerns the matched multi-criteria evaluation of a state- and network-conditioned Fuzzy Q controller with one-step post-Q PCC voltage prediction and selective P(U) activation against a fixed piecewise-linear Q(U) benchmark under identical operating scenarios. The comparison focuses on the resulting trade-off among voltage exposure, protection activity, reactive-power effort, and PV-energy utilization.

To distinguish the contributions of adaptive reactive-power control and selective active power curtailment, six control cases were evaluated under identical operating inputs. Conventional Q(U) + P(U) and Q(U) + shared-P(U) benchmarks were included to distinguish the effects of established combined control, shared selective P(U) logic, and the adaptive Fuzzy Q stage.

The main scientific contributions of this article are as follows:

1. To develop and implement a causal adaptive Fuzzy Q controller and integrate it into a reactive-power-priority Fuzzy Q + P voltage-control architecture that accounts for PCC voltage, its rate of change, PV availability, reactive-power headroom, overvoltage-warning state, and SCR/X/R network conditions while respecting common inverter P–Q capability and protection constraints.
2. To compare six operating cases—Baseline (uncontrolled), fixed Q(U), conventional Q(U) + P(U), Q(U) + shared-P(U), adaptive Fuzzy Q, and the proposed Fuzzy Q + P—across 400 matched 48 h scenarios using PCC voltage performance, modelled protection events, PV-energy utilization, and reactive-power-effort metrics, including direct comparison with conventional combined Q(U) + P(U) control and assessment of the adaptive Fuzzy Q contribution under shared selective P(U) logic.
3. To quantify the incremental effect and selectivity of the P(U) layer by directly comparing Fuzzy Q + P with Fuzzy Q after one-step prediction of the reactive-power response and the resulting residual PCC voltage risk.
4. To determine how the effectiveness of the selective P(U) layer depends on PV availability, load conditions, the coupled SCR/X/R network condition, and the upstream-system scenario.
5. To assess the numerical reliability and scope of the findings through deterministic and runtime verification, real-measurement validation of the equivalent LV feeder-voltage calculation, an independent 400-scenario repeatability assessment, and a limited sensitivity analysis of selected Fuzzy Q + P parameters.

2. Materials and Methods

2.1. Study System and Voltage-Control Problem

The study adopts a balanced three-phase equivalent of a low-voltage distribution system with high photovoltaic penetration, formulated in the per-unit domain. The overall configuration of the study system is presented in Figure 1. The modelled supply chain includes a synthetic 110 kV source-voltage profile, a 110/10 kV transformer with on-load tap-changing (OLTC) voltage regulation, a 10/0.4 kV distribution transformer, an equivalent 0.4 kV network section, and the point of common coupling (PCC), where the local demand and aggregated photovoltaic generation are represented. The 110/10 kV transformer is modelled as an OLTC-controlled voltage-forming stage, while its detailed electromagnetic impedance and loss model are not included. By contrast, the 10/0.4 kV transformer is represented separately through its fixed manual tap setting, series impedance, and no-load branch. A common three-phase base power of S_b = 630 kVA is applied, with nominal line-to-line voltage bases of 110, 10, and 0.4 kV. All simulations, controller implementations, and post-processing were carried out in MATLAB R2025b (The MathWorks, Inc., Natick,

MA, USA). The Mamdani fuzzy inference, membership functions, and controller logic were implemented directly in MATLAB code.

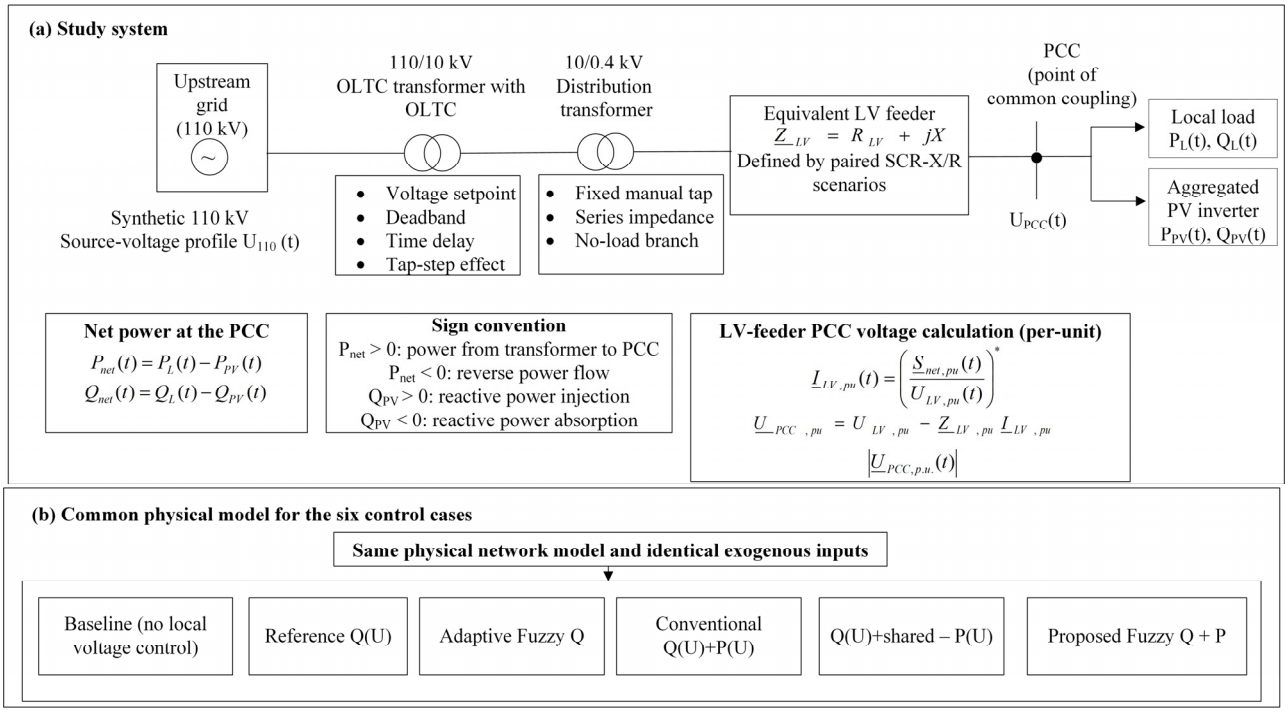


Figure 1. Study system and PCC voltage calculation framework. (**a**) Balanced three-phase equivalent of the modelled 110/10/0.4 kV supply system, equivalent LV feeder, PCC, local load, and aggregated PV inverter, including the adopted power-flow sign convention and PCC voltage calculation. (**b**) Common physical network model used for all six control cases: Baseline, reference Q(U), conventional Q(U) + P(U), Q(U) + shared-P(U), adaptive Fuzzy Q, and proposed Fuzzy Q + P. In panel (**a**), the overlapping white circles denote transformers, the solid lines denote electrical connections, the arrows indicate the reference direction in the schematic, and the superscript asterisk (*) denotes the complex conjugate.

The 10/0.4 kV transformer is assigned a nominal rating of 630 kVA in the scenario generator, whereas the aggregated PV system has a rated active power of 819 kW (1.30 times the transformer rating). These PV/load combinations are intentionally used as voltage-control stress cases and do not imply that the full PV capacity is continuously exported through the transformer. Transformer thermal loading, sustained reverse-power-transfer capability, and compliance with site-specific interconnection requirements were not assessed. Therefore, these simulation cases should not be interpreted as verified permissible continuous operating conditions.

The 0.4 kV network section between the low-voltage terminals of the distribution transformer and the PCC is represented by the equivalent complex impedance:

$$\underline{Z}_{LV,pu} = R_{LV,pu} + jX_{LV,pu}, \quad (1)$$

This formulation makes it possible to vary network strength and impedance properties without altering the detailed feeder topology. The equivalent impedance magnitude is parameterized using a base-referenced short-circuit-ratio index. In this study, the index is defined with respect to the common three-phase system base S_b = 630 kVA as

$$SCR_b = \frac{S_{sc,LV}}{S_b} = \frac{1}{|Z_{LV,pu}|}, \quad (2)$$

where $S_{sc,LV}$ is the short-circuit apparent power associated with the equivalent 0.4 kV network section and $Z_{LV,pu}$ is the corresponding per-unit impedance expressed on the common system base S_b. For brevity, SCR_b is denoted as SCR throughout the remainder of the article. Accordingly, the impedance magnitude used in the model is $|Z_{LV,pu}| = 1/SCR$, while its resistive and reactive components are derived from the specified X/R ratio as

$$R_{LV,pu} = \frac{|Z_{LV,pu}|}{\sqrt{1 + (X/R)^2}}, \quad X_{LV,pu} = (X/R) \cdot R_{LV,pu}, \tag{3}$$

In the present model, SCR is therefore a base-referenced network-strength index used specifically to parameterize the equivalent 0.4 kV section between the transformer LV terminals and the PCC. It should not be understood as the conventional converter-referenced SCR, which is defined using the rated apparent power of the PV inverter, nor as the short-circuit ratio of the entire upstream network as seen from the PCC. Because the impedance of the 10/0.4 kV transformer is represented separately, the MATLAB implementation considers four predefined paired network conditions, (SCR, X/R) = (20, 0.3), (10, 0.5), (5, 1.0), and (3, 2.0), which correspond to progressively larger equivalent LV-network impedance magnitudes with different impedance compositions. The main system, network, and simulation parameters applied in the study are presented in Table 1.

Table 1. Principal system, network, and simulation parameters used in the study.

Parameter	Value/Implementation
System representation	Balanced three-phase quasi-steady-state equivalent
Base apparent power, S_b	630 kVA
Nominal voltage levels	110/10/0.4 kV
10/0.4 kV transformer manual tap	−1 × 2.5%; multiplier 0.975
Aggregated PV rated active power, P_{max}	819 kW
Aggregated inverter rated apparent power, S_{max}	910 kVA
Simulation time step	5 s
Simulation horizon	2 days
LV-network conditions (base-referenced SCR, X/R)	(20, 0.3), (10, 0.5), (5, 1.0), (3, 2.0)

At every time step, the net active and reactive power transferred through the transformer and the corresponding equivalent LV section are obtained from the local load and photovoltaic inverter powers as

$$P_{net}(t) = P_L(t) - P_{PV}(t), \tag{4}$$

$$Q_{net}(t) = Q_L(t) - Q_{PV}(t), \tag{5}$$

Under the adopted sign convention, $P_{net} > 0$ indicates net active power transfer from the transformer to the PCC, while $P_{net} < 0$ corresponds to reverse active power flow driven by local PV generation exceeding the local demand. Positive QPV signifies reactive-power injection by the inverter, whereas negative Q_{PV} denotes reactive-power absorption. Consequently, reactive-power absorption raises Q_{net} and increases the voltage drop across the reactive component of the network impedance. The PCC voltage is obtained directly from the complex power–current–impedance relationship. After normalization by the common base power,

$$\underline{S}_{net,pu}(t) = P_{net,pu}(t) + jQ_{net,pu}(t), \tag{6}$$

the complex current through the equivalent LV section is

$$\underline{I}_{LV,pu}(t) = \left(\frac{\underline{S}_{net,pu}(t)}{\underline{U}_{LV,pu}(t)} \right)^*;, \tag{7}$$

and the PCC voltage is obtained as

$$\underline{U}_{PCC,pu}(t) = U_{LV,pu}(t) - \underline{Z}_{LV,pu}\underline{I}_{LV,pu}(t), \tag{8}$$

$$U_{PCC,p.u}(t) = \left|\underline{U}_{PCC,p.u.}(t)\right|, \tag{9}$$

The transformer low-voltage terminal voltage is used as the zero-angle reference for the equivalent feeder calculation. Accordingly, the PCC voltage is taken directly at each simulation step, and an iterative AC load-flow solution is not used. The model is designed to capture the quasi-steady-state effect of active and reactive-power flows on the PCC voltage, rather than to reproduce the full unbalanced three-phase operating state of a detailed LV network. For physical interpretation, the voltage drop from the transformer LV terminals to the PCC can be approximated by

$$U_{LV} - U_{PCC} \approx \frac{R_{LV}P_{net} + X_{LV}Q_{net}}{U_{LV}}, \tag{10}$$

although this approximation is not used in the numerical calculation of the PCC voltage, it serves to illustrate the core voltage-control issue examined in this study: when photovoltaic generation approaches or surpasses local demand, the reduction and eventual reversal of P_{net} may contribute to voltage rise at the PCC, depending on the feeder impedance, loading conditions, photovoltaic generation level, and available voltage-control actions. This tendency becomes more pronounced under high photovoltaic generation, low local demand, and weak network conditions. In contrast, reactive-power absorption by the PV inverter can increase the voltage drop and thereby reduce overvoltage. Consequently, the effectiveness of reactive-power control depends on both the inverter's available capability and the electrical properties of the network, particularly the short-circuit ratio and the X/R ratio.

Accordingly, the voltage-control problem is posed as the task of keeping the PCC voltage within the specified operating range despite concurrent changes in source voltage, load demand, photovoltaic generation, and network strength, while also adhering to the physical operating constraints of the photovoltaic inverter. The same physical network and voltage calculation model are used for all six examined control cases—Baseline, reference Q(U), conventional Q(U) + P(U), Q(U) + shared-P(U), adaptive Fuzzy Q, and proposed Fuzzy Q + P—so that the observed performance differences can be attributed to the control strategies rather than to differences in the network representations.

2.2. Reference Q(U) Control and Common Inverter Constraints

A fixed piecewise-linear Q(U) controller was implemented as the reactive-power-only reference. To address the need for direct comparisons with combined Volt–Var/Volt–Watt control, two additional benchmarks were included: conventional Q(U) + P(U), combining the fixed Q(U) characteristic with a predefined Volt–Watt curve, and Q(U) + shared-P(U), combining the same fixed Q(U) characteristic with the selective P(U) logic of the proposed controller. These benchmarks were evaluated alongside adaptive Fuzzy Q and the proposed Fuzzy Q + P under the same 400 matched operating scenarios. The uncontrolled baseline was retained as a separate reference case. The comparison with conventional Q(U) + P(U) assesses the performance of the proposed architecture against a standard combined-control approach, whereas the comparison with Q(U) + shared-P(U) isolates the incremental contribution of adaptive Fuzzy Q when the P(U) decision logic is held common. The Fuzzy Q versus Fuzzy Q + P comparison separately evaluates the incremental closed-loop effect of introducing the selective P(U) layer.

At every simulation step k, the voltage sample used by the Q(U) controller, $U_{Q(U)}(k)$, is computed from the active power level allowed by the present inverter protection state and from the actual reactive power obtained in the previous step. This causal formulation

eliminates the need to use the yet-unknown reactive-power command for the current step and therefore does not require fixed-point iteration. The normalized reactive-power reference is obtained from the piecewise-linear characteristic:

$$q_{Q(U)}(t_k) = f_{Q(U)}(U_{Q(U)}(t_k)), \tag{11}$$

defined by the points (0.91, +0.484), (0.95, 0), (1.05, 0), (1.09, −0.484).

Linear interpolation is used between neighbouring points, whereas the end values are preserved beyond the specified voltage range. Under the adopted sign convention, positive Q denotes reactive-power injection and negative Q denotes absorption. Therefore, 0.95 ≤ UQ(U) ≤ 1.05 p.u. defines the Q(U) deadband.

The unrestricted reactive-power command is

$$Q_{raw}(k) = P_{PV,n}, q_{Q(U)}(k), \tag{12}$$

and is limited by the instantaneous inverter capability:

$$Q_{ref}(k) = sat(Q_{raw}(k), -Q_{cap}(k), Q_{cap}(k)), \tag{13}$$

where

$$Q_{cap}(t) = min\left\{0.484P_{PV,n}, \sqrt{S_{max}^2 - P_{inv}^2(k)}\right\}, \tag{14}$$

Here, $P_{inv}(k)$ represents the active power level used for evaluating the corresponding inverter capability. The same symmetric P–Q capability formulation is adopted for all controlled cases, using S_{max} = 910 kVA and $P_{PV,n} = P_{max} = 0.90S_{max}$ = 819 kW. Reactive-power capability is taken as zero whenever either the available or the permitted active power falls below $0.10P_{PV,n}$. This threshold is a numerical modelling assumption, which corresponds to $0.09S_{max}$, rather than a direct grid-code requirement. The reference Q(U) characteristic and the shared inverter P–Q capability constraints used across the compared control methods are shown in Figure 2.

The capability-limited Q reference is processed through two cascaded first-order tracking stages, characterized by time constants of 15 s and 30 s. With the chosen simulation time step of Δt = 5 s, the corresponding discrete coefficients are 0.25 and 1/7, respectively. Both internal states are limited by the instantaneous Q_{cap}, which guarantees that the commanded reactive power remains within the inverter capability represented in the model. Consequently, the 30 s stage functions as a first-order tracking element in the implemented model rather than as an ideal mathematical integrator.

The same voltage-protection, disconnection, reconnection, and post-reconnection active power ramp constraints are enforced across all methods being compared. The adopted voltage thresholds are U > 1.11 p.u. for 600 s, U » 1.15 p.u. for 0.2 s, U < 0.84 p.u. for 3 s, and U « 0.80 p.u. for 2.9 s. After a simulated trip, both active and reactive power are reduced to zero. Reconnection is permitted once the PCC voltage stays continuously within 0.90–1.10 p.u. for 60 s, and then active power recovery proceeds at a rate that does not exceed $0.10P_{PV,n}$ per minute.

Because the simulation employs a 5 s time step, protection delays that are shorter than 5 s are represented at the sampled-data resolution and therefore do not capture sub-second protection dynamics. Accordingly, simulated protection trips should be regarded as comparative indicators within a unified protection framework, rather than as proof of grid-code compliance or as a detailed characterization of the protection behaviour of a particular PV installation.

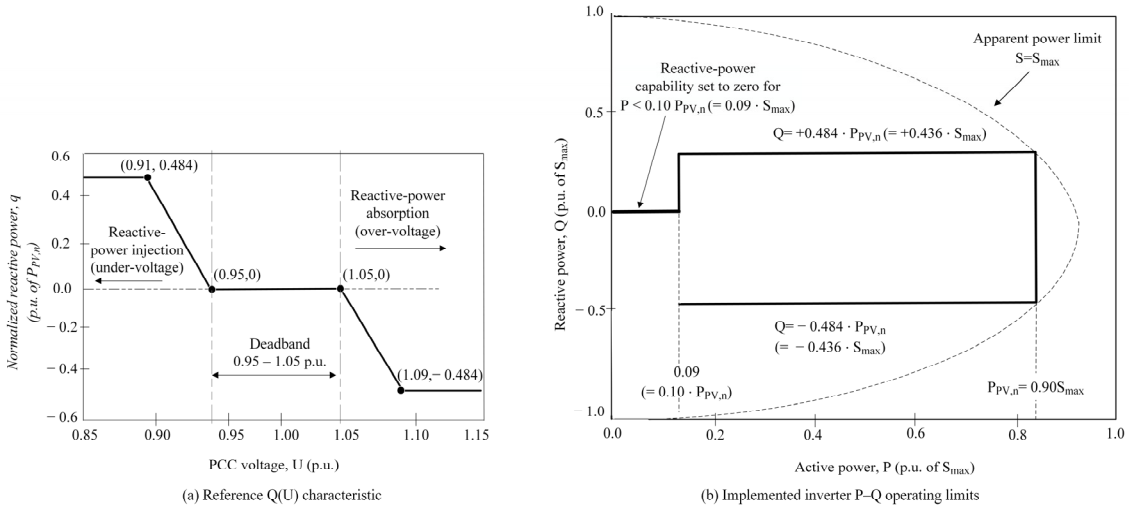


Figure 2. Benchmark Q(U) characteristic and common inverter (P)–(Q) constraints used in the control study. (**a**) Piecewise-linear benchmark Q(U) characteristic with a 0.95–1.05 p.u. deadband. (**b**) Implemented common inverter P–Q constraint, including the apparent-power limit and the model-enforced reactive-power availability threshold. Bold solid lines indicate the implemented Q(U) characteristic and inverter P–Q operating constraints, whereas dashed lines indicate reference thresholds and the apparent-power capability limit.

Conventional Q(U) + P(U) benchmark. The conventional combined controller (Conventional_QU_PU in the MATLAB implementation) retains the fixed Q(U) characteristic and reactive-power tracking dynamics described above and adds a predefined piecewise-linear Volt–Watt P(U) function driven by the sampled PCC voltage. Active power curtailment starts at 1.105 p.u., increases linearly with voltage, and reaches its maximum of 35% at 1.150 p.u. The P(U) characteristic remains fixed across the investigated network conditions. Its decision does not depend on the voltage rate of change, overvoltage-warning timer, reactive-power headroom, SCR/X/R-dependent adaptation, or predicted post-Q voltage. This benchmark provides a conventional combined-control reference against which the operational value of the proposed architecture can be assessed.

Q(U) + shared-P(U) ablation benchmark. The second combined controller (ESO_QU_PU in the MATLAB implementation) retains the same fixed Q(U) reactive-power characteristic and tracking dynamics but applies the selective P(U) activation logic used in the proposed Fuzzy Q + P controller. The P(U) decision is based on the predicted PCC voltage following the one-step Q response, together with the associated voltage risk conditions, reactive-power capability utilization, and overvoltage-warning information. The corresponding P(U) thresholds and curtailment limits follow the same network-conditioned settings as the proposed controller. This benchmark isolates the contribution of the adaptive Fuzzy Q stage by keeping the selective P(U) mechanism common to both control architectures. Both additional benchmarks use the common inverter P–Q capability constraints, active power ramp limits, and protection, disconnection, reconnection, and recovery logic.

2.3. Adaptive Fuzzy Q Control

The adaptive Fuzzy Q controller forms the reactive-power control stage of the proposed method and is also tested separately to distinguish the effect of adaptive reactive-power regulation prior to activating the P(U) layer. The controller uses a Mamdani-type fuzzy inference system with min–max aggregation and centroid defuzzification. Positive Q indicates reactive-power generation, whereas negative Q indicates reactive-power absorption. In the Fuzzy Q-only scenario, no controller-driven active power curtailment is performed;

however, active power may still be constrained by the shared protection, disconnection, reconnection, and post-reconnection ramp logic.

At each simulation step k, the time-varying controller information is represented by

$$x_k = \left[U_k, \quad \dot{U}_k, \quad p_{PV,k}, \quad m_{Q,k}, \quad \theta_k, \quad SCR, \quad X/R\right]; \tag{15}$$

where U_k is the sampled PCC voltage, $\dot{U}_k$ is its filtered rate of change, $p_{PV,k} = P_{PV,avail,k}/P_{PV,n}$ is the available-PV-power ratio, $m_{Q,k}$ is the remaining reactive-power headroom, and θ_k is the normalized overvoltage-warning-timer state. Each network scenario also includes a fixed SCR–X/R pair that serves as the network-adaptation context rather than as a time-varying measurement. In this study, SCR and X/R are predefined network condition descriptors and are not estimated online; online estimation of these parameters is beyond the scope of this study. In this study, the term adaptive refers to the state- and network-condition-dependent modification of the control action; it does not imply online estimation of SCR or X/R. The reactive-power headroom is assessed as

$$m_{Q,k} = 1 - \min\left(\frac{|Q_{k-1}|}{Q_{cap,k}}, 1\right); \tag{16}$$

with $m_{Q,k} = 0$ when $Q_{cap,k} = 0$, where $Q_{cap,k}$ is the instantaneous inverter capability defined in Section 2.2. The warning state is

$$\theta_k = \frac{T_{warn,k}}{600}; \tag{17}$$

where $T_{warn,k}$ accumulates while $U_k \geq 1.10$ p.u. and is reset when the voltage falls below this threshold. The ratio is not clipped at unity.

The voltage-rate signal is determined in a causal manner from the sampled PCC voltage and from the final PCC voltage obtained in the preceding simulation step:

$$\dot{U}_k^{raw} = \frac{60\left(U_k - U_{k-1}^{final}\right)}{\Delta t}; \tag{18}$$

and filtered using a first-order discrete filter,

$$\dot{U}_k = \dot{U}_{k-1} + \alpha_d\left(\dot{U}_k^{raw} - \dot{U}_{k-1}\right); \quad \alpha_d = \frac{\Delta t}{T_d + \Delta t}; \tag{19}$$

The nominal derivative-filter time constant is given by Td = 30 s. Under very weak network conditions, defined as SCR ≤ 3 or X/R ≥ 2, it is increased to 90 s, and the filtered derivative is constrained to ±0.03 p.u./min. Separately filtered derivative states are then employed by the dynamic and safety layers. The fuzzy inference stage converts the operating state into a normalized reactive-power command $q_{F,k}$, which is limited to

$$-0.484 \leq q_{F,k} \leq 0.484; \tag{20}$$

using eight output sets ranging from maximum generation to maximum absorption and a defuzzification grid step of 0.002. SCR and X/R affect both rule activation and the subsequent network-adaptive scaling of the absorptive commands. For SCR ≤ 3, 3 < SCR ≤ 5, and SCR > 5, the associated SCR gains are 1.35, 1.15, and 1.00, respectively. For 1 ≤ X/R < 2 and X/R ≥ 2, additional gains of 1.10 and 1.20 are applied. When both adaptations are active, their effects are combined, whereas positive reactive-power commands are not amplified.

A dynamic layer then adjusts the magnitude of the reactive-power control action based on the PCC voltage level, the voltage trajectory, the available-PV capacity, and the accumulated overvoltage risk. To this end, a trend-based voltage extrapolation is constructed as

$$U_{trend,k} = U_k + T_{pred}\dot{U}_k, \quad T_{pred} = 5\text{min}; \tag{21}$$

This quantity is used exclusively to evaluate the short-term voltage trend in the Fuzzy Q dynamic layer. Accordingly, it must be separated from the one-step Q-response-based PCC voltage prediction presented in Section 2.4 when determining whether the P(U) layer should be activated. The dynamic-aggressiveness state is smoothed with a 30 s first-order filter; it enhances absorption when high-voltage levels rise and, at the same time, reduces unnecessary reactive-power exchange in the normal-voltage range.

The following safety layer prevents inadequate reactive-power absorption when operating under elevated-voltage conditions. The reference Q(U) characteristic specified in Section 2.2 is applied internally as a safety limit: the fuzzy command cannot require weaker absorption when $U_k \geq 1.090$ p.u., or when $U_k \geq 1.075$ p.u. during a voltage rise. The maximum normalized absorption, $q = -0.484$, is enforced when $U_k \geq 1.110$ p.u., or when $\theta_k \geq 0.20$. An absorption-hold mechanism introduces hysteresis following elevated-voltage events and prevents a rapid release of reactive power. Under extremely weak network conditions, the safety thresholds are triggered earlier, and the hold logic is made more conservative.

The final normalized command is transformed into reactive power, and it is constrained by the instantaneous P–Q capability specified in Section 2.2. Reactive-power control is turned off whenever either the available photovoltaic power or the active power operating point allowed by protection is less than $0.10P_{PV,n}$. The capability-limited command is then routed through two cascaded first-order reactive-power dynamics with time constants of 15 s and 30 s. For each dynamic state, the inverter capability imposes the governing constraint.

All controller actions, reactive-power dynamics, inverter capability, and protection states advance causally once per simulation step of $\Delta t = 5$ s. No fixed-point iteration is performed within the same step for the voltage–reactive-power coupling. After a protection trip, the Fuzzy and Q dynamic states are reset and kept inactive while the inverter is disconnected; following reconnection, reactive-power control restarts from zero, whereas active power continues to satisfy the shared reconnection-ramp constraint. The Mamdani inference system includes 23 rules and eight active output sets covering normalized reactive-power commands from maximum generation to maximum absorption. Triangular and trapezoidal membership functions are applied to the voltage, voltage trend, PV availability, reactive-power headroom, warning state, and network condition inputs. The rule base is designed to advance the control objective of progressively increasing reactive-power absorption as voltage increases, characterized by an upward voltage trend, while accounting for diminishing reactive-power headroom as a capability constraint, accumulated overvoltage risk, and less favourable network conditions, while also preventing unnecessary reactive-power exchange within the normal-voltage region. All fuzzy-controller rule definitions, membership-function breakpoint values, scaling factors, and related thresholds were set prior to the main comparative study and then applied without modification across the corresponding scenario matrix. The full numerical controller parameterization is preserved in the MATLAB implementation and may be supplied to reviewers or made available by the corresponding author upon reasonable request for purposes of verification and reproducibility.

2.4. Control Logic of the Proposed Fuzzy Q + P Method

The proposed Fuzzy Q + P controller builds on the adaptive Fuzzy Q method presented in Section 2.3 by incorporating a selective active power curtailment layer. Its core concept is reactive-power prioritization: the anticipated short-term impact of the Fuzzy Q command is assessed before any active power reduction is considered. Consequently, P(U) is not used as a general regulator of voltage quality; instead, it serves as a selective pre-trip mitigation mechanism when an elevated overvoltage risk persists after the predicted reactive-power response.

At every 5 s sampling instant, the controller first obtains the sampled PCC voltage based on the current inverter state. In the Fuzzy Q + P implementation, the sampled active power state contains the P(U) curtailment carried over from the previous time step, while the new P(U) command is then computed relative to the active power limit allowed by the current protection and reconnection state. The sampled PCC voltage is also used to determine the filtered voltage rate of change and the auxiliary overvoltage risk timer. The latter accumulates whenever the sampled PCC voltage is at or above 1.10 p.u., and it is measured against a 600 s interval.

The adaptive Fuzzy Q algorithm produces the reactive-power reference, initially limited by the inverter P–Q capability associated with the sampled active power state. The reactive-power output is then forecast one sampling step ahead by carrying forward the same 15 s and 30 s reactive-power dynamics employed by the controller, while not updating their internal states. The predicted reactive power is then applied within the network model to determine the intermediate PCC voltage U_{afterQ}. Consequently, the P(U) decision relies on the voltage anticipated after the immediate Fuzzy Q response and before the subsequent P(U) action.

The causal sequence of the proposed reactive-power-priority Fuzzy Q + P controller is summarized in Figure 3.

The P(U) activation logic relies on U_{afterQ}, the filtered voltage trend, the pre-P(U) reactive-power saturation ratio, and the overvoltage risk timer. Three voltage risk regions and the corresponding P(U) activation conditions are summarized in Table 2.

Table 2. Voltage risk regions and P(U) activation conditions in the proposed Fuzzy Q + P controller.

Predicted Voltage U_{afterQ}	Additional Risk Condition
U_{start} to <1.110 p.u.	timer ratio ≥ 0.05 or dU/dt ≥ 0.0005 p.u./min
1.110 to <1.130 p.u.	Q-capability utilization ratio ≥ 0.85 or timer ratio ≥ 0.05
≥1.130 p.u.	residual overvoltage risk gate satisfied directly; the resulting curtailment magnitude remains determined by the Q-saturation and timer terms

In standard grid operating conditions, U_{start} equals 1.105 p.u., and the maximum active power curtailment is 0.35 p.u. In the very-weak-grid mode, which is defined by SCR ≤ 3 or X/R ≥ 2, these values are updated to U_{start} = 1.100 p.u. and a maximum curtailment of 0.50 p.u., respectively. A distinct minimum activation-voltage limit of 1.095 p.u. is still applied as an additional control safeguard; consequently, the effective voltage activation requirement is assessed against the larger value between the relevant U_{start} setting and this minimum limit. With the nominal parameterization, this floor stays below both choices of U_{start}, so it does not control the activation of P(U) in the nominal scenarios; its role is limited to providing an additional safety margin when lower activation settings are adopted.

When the relevant activation conditions are met, the curtailment magnitude increases continuously as the required predicted voltage rises and as the larger of the reactive-power saturation requirement and the overvoltage timer requirement increases. The voltage contribution attains its full value at 1.150 p.u.; the Q-saturation contribution ranges from ratios of 0.85 to 1.00, while the timer contribution ranges from 0.05 to 0.50. Accordingly, meeting the voltage risk condition by itself does not necessarily result in a nonzero active power curtailment command.

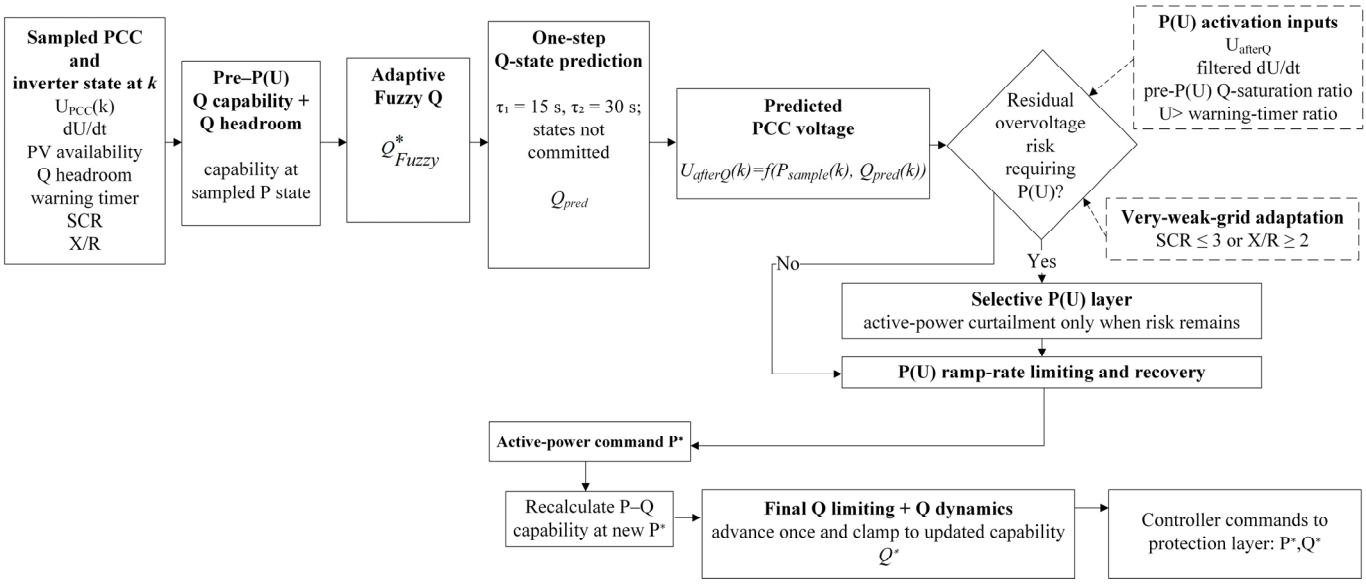


Figure 3. Proposed reactive-power-priority Fuzzy Q + P control architecture. Solid arrows indicate the main signal and control-flow paths, whereas dashed boxes denote auxiliary activation or adaptation inputs. The asterisk (*) denotes commanded or reference values.

Once the P(U) active power limit has been determined, the inverter's P–Q capability is recomputed using the reduced active power command. The fuzzy Q reference is then constrained by this updated capability; afterward, the two reactive-power dynamic states are advanced exactly once and each is individually limited to the resulting capability. The resulting P and Q commands are subsequently assessed by the shared inverter protection-state machine. If a protection trip occurs, the delivered active and reactive powers are set to zero, and the associated controller states are reset.

This causal sequence captures the key characteristic of the proposed method: reactive-power action is assessed first, while active power curtailment is applied only in a targeted manner when the predicted post-Q state suggests a continued risk of critical overvoltage. The P(U) thresholds used in this work are specific to the study's MATLAB controller parameters rather than reflecting normative P(U) settings.

2.5. Scenario Matrix and Performance Metrics

A paired factorial scenario matrix was employed to evaluate all control strategies under identical input conditions. Specifically, four upstream-system scenarios, five load profiles, four low-voltage network equivalents, and five available-PV-power profiles were integrated, producing 400 scenario cases for each control strategy:

$$N_{SC} = 4 \times 5 \times 4 \times 5 = 400, \quad (22)$$

The scenario dimensions, their levels, and the implemented cases are summarized in Table 3.

All six control cases were evaluated using identical upstream-system, load, network, and PV inputs. The results were paired by scenario identifier, and consistency checks confirmed complete matching across the compared cases. The SCR and X/R values served as coupled descriptors of each predefined LV-network equivalent and were not varied as independent factorial dimensions. Each case corresponds to a separate 48 h simulation window. Consequently, energy totals accumulated across the 400-case matrix are scenario-level aggregates and must not be interpreted as a continuous 800-day record or annual energy yield. Since the input-profile libraries are reused across factorial combinations, the

400 cases constitute a fixed comparative scenario set rather than statistically independent Monte Carlo replications.

Table 3. Scenario matrix, control cases, and simulation settings.

Scenario Dimension	Levels	Implemented Cases
Upstream-system scenario	4	HighVoltageWide; NominalVoltage; LowVoltageWide; UnstableVoltage
Load	5	NoLoad; LightLoad; IntensiveLoad; OverloadLoad; UnstableLoad
LV-network equivalent	4	StrongNetwork (SCR = 20, X/R = 0.3); MediumNetwork (10, 0.5); WeakNetwork (5, 1.0); VeryWeakNetwork (3, 2.0)
Available-PV power	5	PV000; PV025; PV075; PV100; PVU075 (cloud-variable profile)
Scenario cases per strategy	400	Full factorial combination of the four input dimensions
Control strategies	6	Baseline (no local voltage control); Reference Q(U); Conventional Q(U) + P(U); Q(U) + shared-P(U); Adaptive Fuzzy Q; Proposed Fuzzy Q + P
Total model-case executions	2400	400 matched scenarios × 6 evaluated control cases
Simulation horizon/time step	—	48 h per case/5 s

Each upstream-system scenario links a single 110 kV source-voltage profile to one fixed realization of the OLTC parameters and the electrical parameters of the 10/0.4 kV transformer. For the predefined upstream-system realizations, the OLTC setpoint was adjusted within 1.075–1.095 p.u., using a 0.008–0.015 p.u. deadband and a 300 s delay, whereas the 10/0.4 kV transformer parameters were generated within u_k = 4–6%, P_k = 4–10 kW, P_0 = 0.6–2.0 kW, and i_0 = 0.8–1.6%. Consequently, this dimension is handled as a predefined upstream-system condition rather than as an isolated source-voltage factor. In all cases, the 10/0.4 kV transformer manual tap was kept constant at −1 × 2.5%.

The overall scenario-based comparative assessment framework, including scenario generation, evaluation of the six control cases, multi-criteria performance assessment, and matched scenario-level comparisons, is summarized in Figure 4.

Performance was evaluated using physically interpretable metrics organized into four categories: PCC voltage performance, modelled protection operation, PV-energy utilization, and reactive-power control effort. Voltage performance was described by the voltage extremes, the time spent above selected voltage thresholds, and the root-mean-square error with respect to the predefined common comparison target U_{target}:

$$RMSE_V = \sqrt{\frac{1}{N}\sum_{k=1}^{N}\left(U_{PCC,k} - U_{target}\right)^2}, \quad (23)$$

Here, U_{target} = 1.035 p.u. represents the fixed, model-wide comparison reference that is applied identically across all strategies; it is not to be understood as a statutory voltage limit or a protection threshold. For a descriptive voltage threshold Uth, the accumulated exceedance duration was computed as

$$T_{>U_{th}} = \frac{\Delta t}{3600}\sum_{k=1}^{N} I(U_{PCC,k} > U_{th}), \quad (24)$$

The 1.10 p.u. level was used solely as a descriptive elevated-voltage exposure threshold and was not treated as a protection-trip criterion. Protection performance was assessed separately from simple threshold occupancy by using the event-based outputs of the implemented time-delay protection logic, including the total number of trip events. For the active protection profile, continuous exposure at the first overvoltage threshold (1.11 p.u.) was also evaluated after the implemented delay. This separation avoids incorrectly equating

voltage-threshold exceedance with the actual modelled protection operation. PV-energy performance was evaluated based on the available and delivered active power. The generated and undelivered energies were calculated as

$$E_{gen} = \frac{\Delta t}{3600}\sum_{k=1}^{N} P_{PV,k}^{act}, \quad E_{und} = \frac{\Delta t}{3600}\sum_{k=1}^{N}\left(P_{PV,k}^{avail} - P_{PV,k}^{act}\right) \tag{25}$$

The corresponding fraction of unserved energy was used to quantify the active-energy cost associated with voltage regulation and protection-related unavailability. For Fuzzy Q + P, the model also captures the effective P(U) curtailment energy and the effective P(U) activation time, enabling the contribution of the active power layer to be analyzed separately from the total unserved energy.

Reactive-power utilization was represented by the absolute reactive-energy effort:

$$E_Q = \frac{\Delta t}{3600}\sum_{k=1}^{N}\left|Q_{PV,k}\right|, \tag{26}$$

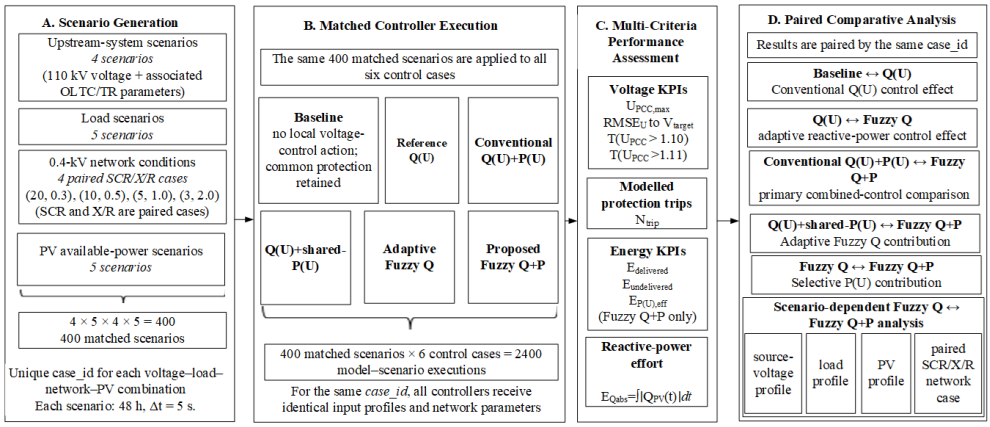


Figure 4. Scenario-based comparative assessment framework. (**A**) Scenario generation based on upstream-system, load, LV-network, and available-PV-power conditions. (**B**) Matched execution of the six control cases using identical scenario inputs. (**C**) Multi-criteria performance assessment based on voltage, protection, energy, and reactive-power-effort metrics. (**D**) Paired comparative analysis of the control strategies using identical scenario identifiers. Double-sided arrows indicate pairwise comparisons between two control strategies under the same matched scenario conditions.

The duration of reactive-power saturation and the Q dynamic indicators were retained as secondary diagnostic metrics for interpreting controller behaviour rather than as independent measures of overall superiority. Conventional Q(U) + P(U) was adopted as the principal combined-control benchmark for assessing the proposed Fuzzy Q + P architecture. The Q(U) + shared-P(U) comparator was used to isolate the incremental contribution of adaptive Fuzzy Q under the same selective P(U) decision mechanism. The original Q(U) reference was retained to assess performance relative to reactive-power-only voltage regulation, while the direct Fuzzy Q versus Fuzzy Q + P comparison quantified the incremental effect of introducing the selective active power curtailment layer. Comparative conclusions were based on the individual physical performance measures without applying a single composite ranking.

2.6. Verification, Repeatability, Sensitivity, and Real-Data Validation Protocol

The numerical implementation was verified before the performance results were interpreted. Forty-three deterministic PASS/FAIL software checks were used to verify the PCC voltage calculation, network and per-unit transformations, causal execution of the implemented controllers, inverter P–Q capability, reactive-power dynamics, protection

and reconnection sequences, selected energy-accounting invariants, and comparative-data integrity. The evidence-integrity checks confirmed complete and unique scenario records, matching scenario metadata, and finite required performance indicators for all six control cases. A separate time-step convergence assessment was conducted for selected model and operating scenarios using finer sampling intervals and predefined acceptance criteria, including the stability of paired performance-difference directions across discretization. In addition, for the 1600 model–scenario executions of the original four control cases, stepwise runtime-validity checks were applied that required finite causal states, consistency between the stepwise voltage calculation and the corresponding network-model recompilation within numerical tolerance, and agreement of the resulting reactive power with the instantaneous inverter capability. A simulation that failed any of these checks was rejected as an invalid model execution.

The repeatability of the principal comparative trends was examined using a separately generated synthetic scenario matrix. The controller formulation and nominal parameter set were held fixed prior to this independent repeatability assessment and were not re-tuned using the secondary scenario matrix. A different random-number base seed (7300) was used to produce new realizations of the four upstream-system scenarios, including their source voltage, OLTC, and transformer parameters, along with new load and available-PV profiles, while keeping the same scenario definitions, parameter ranges, four predefined SCR–X/R network cases, and four original control strategies (Baseline, Q(U), Fuzzy Q, and Fuzzy Q + P). The resulting matrix again contained $4 \times 5 \times 4 \times 5 = 400$ matched scenarios. Within this repeatability matrix, these four controllers were tested under identical exogenous inputs and network conditions. The cross-matrix assessment determined whether the principal paired performance trends found in the main study were reproduced; no statistical significance or automatic acceptance criterion was imposed for trend agreement, and the scenario cases were not treated as statistically independent Monte Carlo replications.

An additional limited parameter-sensitivity evaluation was carried out for the final Fuzzy Q + P controller, using the same secondary scenario matrix. The nominal P(U) voltage parameters—namely the normal-grid start threshold $U_{start} = 1.105$ p.u., the very-weak-grid start threshold $U_{start} = 1.100$ p.u., and the minimum activation-voltage floor $U_{min,act} = 1.095$ p.u.—were collectively shifted to a later-activation set (1.110, 1.105, 1.100) p.u. and to an earlier-activation set (1.100, 1.095, 1.090) p.u., respectively.

In a separate perturbation, the SCR threshold used to activate the very-weak-grid parametrization was raised from 3.0 to 3.5, while the associated criterion of X/R = 2.0 remained unchanged. All other model and controller settings were kept the same. Accordingly, this procedure is understood solely as a local sensitivity check of selected parameters, rather than as a global robustness analysis, controller optimization, or a demonstration of insensitivity across a continuous parameter space.

An additional benchmark sensitivity analysis was conducted using five distinct fixed Q(U) characteristics with different slopes and deadbands. Reference Q(U) and conventional Q(U) + P(U) were evaluated across the same 400 matched 48 h scenarios for each characteristic. The proposed Fuzzy Q + P controller remained unchanged and served as a common comparator. The investigated characteristics and performance results are provided in Table A1 (Appendix A).

A separate exploratory P(U) parameter-sensitivity sweep was conducted using 25 controller settings evaluated across the same 12 selected matched 48 h scenarios. For each setting, cumulative effective P(U)-curtailed energy, critical-overvoltage duration above 1.11 p.u., and modelled protection-trip events were recorded. This analysis was performed separately from the 400-scenario main and repeatability assessments and was not intended to establish globally optimal controller parameters.

A supplementary bounded one-at-a-time (OAT) sensitivity analysis was conducted for 10 controller-parameter groups at five predefined levels around their nominal settings using 12 selected high-PV (PV100) scenarios, each simulated for 48 h. The tested parameter ranges and resulting performance variations are summarized in Table A2 (Appendix A). This analysis provides a local parameter-sensitivity assessment and does not quantify parameter interactions or establish global robustness.

A separate discrete SCR–X/R sensitivity sweep was performed outside the main 400-scenario matrix. The base-referenced SCR was varied independently across seven values (3, 4, 5, 7.5, 10, 15, and 20), and X/R across five values (0.3, 0.5, 1.0, 1.5, and 2.0), yielding 35 network–parameter combinations. Eight operating scenarios (Cases 9, 14, 19, 34, 109, 119, 219, and 319) were selected a priori. All eight represented maximum PV availability (PV100); seven used NoLoad conditions and one used LightLoad conditions, covering four upstream-voltage profiles. Each network combination was evaluated using the same eight operating scenarios for conventional Q(U) + P(U) and the proposed Fuzzy Q + P controller, resulting in 560 model–scenario simulations. Mean paired differences were calculated as Fuzzy Q + P minus conventional Q(U) + P(U) for critical-overvoltage duration above 1.11 p.u. and modelled protection-trip counts (Figure A1, Appendix B). No interpolation was applied. This analysis represents a discrete, high-PV operating-condition sensitivity assessment and does not establish robustness across the continuous SCR–X/R domain.

Finally, the physical voltage calculation step for the equivalent 0.4 kV feeder model was evaluated against measurements from an actual operating site. The measured mean line-to-line voltage at Bus A, along with the simultaneous active- and reactive-power flows at the same location, were used as model inputs to compute the voltage at Bus B. The measured Bus B voltage was not used in the calculation; it served only as the reference quantity for comparison. Measurements were aligned on the shared 5 s time grid, and only fully synchronized samples were kept, with no interpolation. The feeder resistance and reactance were fixed using the available technical data and were not calibrated using the measured Bus B voltage. Agreement was assessed with residual-based error metrics, including mean absolute error, root-mean-square error, and bias, together with additional correlation analyses and threshold-state diagnostics. This real-data assessment validates only the equivalent low-voltage feeder-voltage calculation within the observed operating range; it does not amount to experimental validation of the Q(U), Fuzzy Q, Fuzzy Q + P controllers, their P(U) activation logic, or the implemented protection functions.

3. Results

3.1. Model Verification and Real-Data Validation

Before interpreting the comparative controller results, the numerical implementation was verified using the deterministic and runtime checks specified in Section 2.6. All 43 deterministic PASS/FAIL software checks passed. For the original four control strategies, all 1600 model–scenario executions met the predefined stepwise runtime-validity criteria, with no invalid simulation steps or violations of instantaneous inverter P–Q capability. The causal PCC voltage calculations were consistent with the corresponding network-model recalculations within numerical tolerance. The two additional combined Q(U) + P(U) benchmarks contributed 800 further executions, resulting in 2400 model–scenario executions across six control strategies. For these additional benchmarks, the evidence-integrity checks confirmed complete scenario coverage, matching scenario metadata, and finite required performance indicators. The stepwise runtime-validity findings are restricted to the original 1600 executions. These results demonstrate numerical consistency and comparative-data integrity but do not establish experimental validation of the controllers.

Therefore, the physical validation was carried out separately for the equivalent 0.4 kV feeder-voltage calculation. The uncalibrated model was assessed using 81,951 synchronized 5 s samples, which correspond to approximately 113.8 h of data collected at the real operating site. The contemporaneous measured mean line-to-line voltage at Bus A and the active- and reactive-power flow at the same location were used as model inputs, while the measured voltage at Bus B was kept for comparison. The feeder parameters, R = 0.04554 Ω and X = 0.01440 Ω, were taken from the available technical documentation and were not fitted to the measured Bus B voltage. The agreement between the measured and calculated Bus B voltages, together with the corresponding ordered voltage residuals, is presented in Figure 5.

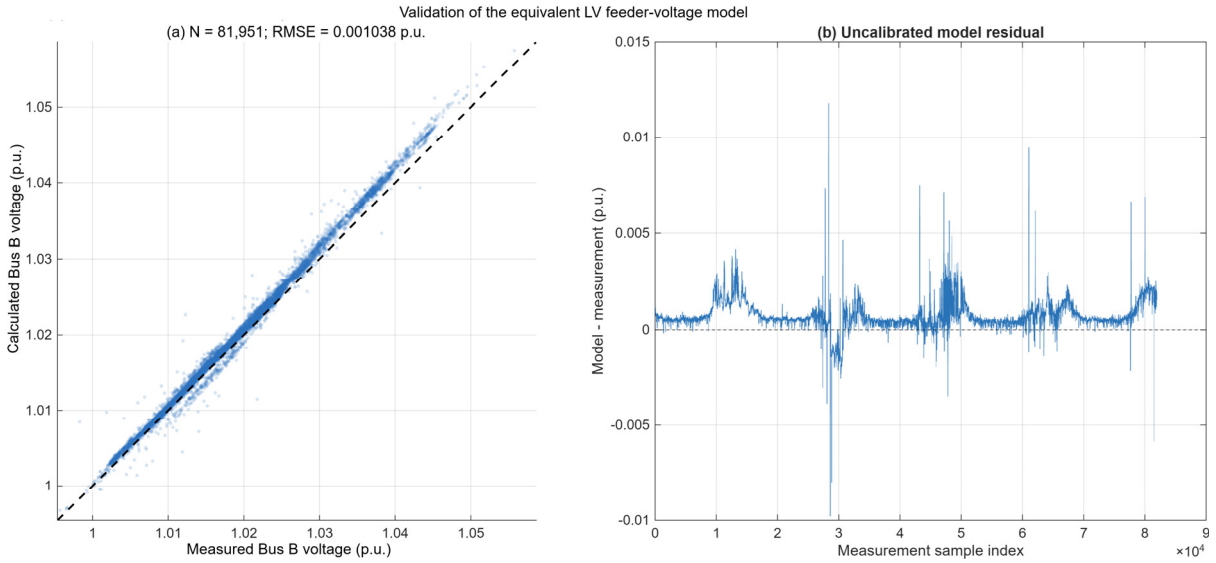


Figure 5. Real-data validation of the uncalibrated equivalent 0.4 kV feeder-voltage calculation. (**a**) Measured versus calculated mean line-to-line voltage at Bus B for 81,951 synchronized 5 s samples (RMSE = 0.001038 p.u.). Blue markers represent individual synchronized samples; darker blue regions result from overlapping data points and do not represent different data categories. The dashed line represents ideal agreement (y = x). (**b**) Voltage residuals ($U_{calc} - U_{measured}$) plotted against the measurement-sample index. The dashed horizontal line indicates zero residual. The calculation uses contemporaneous measured Bus A voltage and feeder active- and reactive-power flows as inputs. This assessment validates the equivalent LV feeder-voltage calculation within the observed operating range and does not constitute experimental validation of the investigated voltage-control strategies.

As summarized in Table 4 and Figure 5, the calculated Bus B voltage showed low overall errors when compared with the measurements. Specifically, the MAE was 0.000812 p.u. (0.325 V), the RMSE was 0.001038 p.u. (0.415 V), and the mean residual $U_{calc} - U_{measured}$ was +0.000725 p.u. (+0.290 V). The Pearson correlation coefficient was 0.9976, with R2 = 0.9864. In comparison with the basic $U_B = U_A$ reference, for which the RMSE was 0.004054 p.u. (1.622 V), incorporating the equivalent feeder-voltage drop lowered the RMSE by 74.39%. All valid synchronized samples were included in these aggregate error metrics. The measurement-chain uncertainty was not quantified because analyser and CT/VT accuracy data were unavailable for the validation configuration; therefore, the reported residuals reflect the combined discrepancy between the equivalent model and the measurement system.

Table 4. Real-data validation metrics for the uncalibrated equivalent 0.4 kV feeder-voltage model.

Metric	Value
Valid samples, N	81,951
MAE	0.000812 p.u. (0.325 V)
RMSE	0.001038 p.u. (0.415 V)
Bias	+0.000725 p.u. (+0.290 V)
Pearson *r*	0.9976
R^2	0.9864
$U_B = U_A$ reference RMSE	0.004054 p.u. (1.622 V)
RMSE reduction relative to $U_B = U_A$	74.39%

During the validation period, the measured voltage at Bus B ranged only from 0.9954 to 1.0569 p.u., and there were no samples exceeding 1.10 or 1.11 p.u. Accordingly, the real-data findings support only the equivalent feeder-voltage computation within the operating range that was observed. They do not amount to experimental validation of the Q(U), Fuzzy Q, Fuzzy Q + P controllers, the selective P(U) activation logic, the protection functions, or their behaviour in the higher-voltage region addressed by the synthetic scenarios. Furthermore, because the measured voltage at Bus A and the P/Q power flows are used as simultaneous model inputs, this evaluation should be understood as validation of the feeder-voltage-drop calculation rather than as an independent prediction of the voltage at Bus B. Since the measured voltage at Bus A is applied directly as an input to the model, this validation does not evaluate the upstream OLTC or transformer models. This constraint is significant because the manuscript explicitly distinguishes physical model validation from controller validation.

3.2. Multi-Criteria Comparison of the Voltage-Control Methods

The six operating cases were evaluated using the same set of 400 matched 48 h scenarios. Because the scenario matrix constitutes a fixed comparative framework rather than statistically independent Monte Carlo realizations, the findings are interpreted descriptively, with every scenario assigned equal weight. Table 5 summarizes the principal voltage performance, protection, PV-energy, and reactive-power-effort metrics for all six operating cases.

As shown in Table 5, all five controlled strategies substantially improve critical-overvoltage exposure and modelled protection-trip indicators relative to the uncontrolled baseline. The proposed Fuzzy Q + P controller achieved the lowest mean duration above 1.11 p.u. (1.7612 h/scenario). Compared with reference Q(U), this represents a reduction of approximately 2.20%, accompanied by 3.98% fewer modelled protection trips. However, these benefits required 48.33% greater reactive-power effort and resulted in 0.23% lower generated PV energy. Furthermore, the mean duration above 1.10 p.u. increased by 2.99%, demonstrating that the proposed strategy does not improve all voltage performance indicators simultaneously.

Compared with conventional Q(U) + P(U), the proposed Fuzzy Q + P controller reduced critical-overvoltage duration by 1.17%, but produced 1.59% more modelled protection trips, 0.57% less generated PV energy, and 46.89% greater reactive-power effort. The Q(U) + shared-P(U) strategy achieved the lowest mean protection-trip count (7.4650 events/scenario) and the highest generated PV energy (5.4663 MWh/scenario), whereas Adaptive Fuzzy Q produced the lowest voltage RMSE (0.099148 p.u.). Compared with Q(U) + shared-P(U), the proposed method achieved only a small additional reduction in critical-overvoltage duration (0.0028 h/scenario), accompanied by higher protection activity and reactive-power effort. Overall, these findings indicate that the proposed architecture provides a modest improvement in critical-overvoltage mitigation under the investigated scenarios rather than universal superiority over established combined-control strategies. Protection-trip comparisons remain subject to the numerical time-step limitations discussed in Section 3.5.

Table 5. Multi-criteria performance of six voltage-control strategies across 400 matched 48 h scenarios (mean values per scenario).

Control Strategy	Mean Maximum U_{PCC} (p.u.)	RMSE to Target (p.u.)	T(U_{PCC} > 1.10) (h/Scenario)	T(U_{PCC} > 1.11) (h/Scenario)	Modelled Trips (Events/Scenario)	Generated PV Energy (MWh/Scenario)	Absolute Q Effort (MVArh/Scenario)
Baseline (no local control)	1.1495	0.105395	3.7887	2.9370	22.4900	4.6567	0.0000
Q(U)	1.1394	0.099792	2.0783	1.8007	7.9825	5.4429	1.5326
Conventional Q(U) + P(U)	1.1386	0.099786	2.1358	1.7821	7.5450	5.4614	1.5476
Q(U) + shared − P(U)	1.1386	0.099791	2.1467	1.7640	7.4650	5.4663	1.5507
Adaptive Fuzzy Q	1.1397	0.099148	2.0729	1.7986	8.1850	5.4082	2.2606
Proposed Fuzzy Q + P	1.1390	0.099155	2.1404	1.7612	7.6650	5.4301	2.2733

Note: RMSE values represent the means of individual scenario RMSEs relative to U_{target} = 1.035 p.u. Voltage exposure thresholds of 1.10 and 1.11 p.u. are descriptive metrics and must not be interpreted as protection-trip criteria. Modelled trip counts are sensitive to simulation time-step resolution. Reactive-power effort is calculated as $\int |Q| dt$.

The supplementary Q(U) characteristic sensitivity analysis (Table A1, Appendix A) showed that the mean critical-overvoltage duration ranged from 1.7987 to 1.8227 h/scenario for reference Q(U) and from 1.7810 to 1.7968 h/scenario for conventional Q(U) + P(U). The unchanged proposed Fuzzy Q + P controller achieved 1.7612 h/scenario, outperforming all five tested benchmark characteristics in this specific voltage exposure metric. However, the proposed controller required greater reactive-power effort and did not outperform the conventional combined controllers in modelled protection-trip counts or generated PV energy. These findings support the proposed method's advantage in critical-overvoltage mitigation within the tested benchmark configurations, without establishing universal superiority over optimally tuned Q(U) controllers.

3.3. Incremental Effect of the P(U) Layer

To measure the incremental closed-loop impact of the active power layer, Fuzzy Q + P was evaluated directly against Fuzzy Q using the same 400 matched scenarios. Both variants rely on the same causal adaptive Fuzzy Q core and shared inverter protection logic; Fuzzy Q + P additionally implements the selective P(U) layer after the predicted one-step reactive-power response and then recomputes the inverter's P–Q capability based on the resulting active power command.

Relative to Fuzzy Q-only control, enabling selective P(U) reduced the accumulated duration above 1.11 p.u. from 719.422 to 704.467 h across the 400-case matrix (−14.956 h; −2.08%) and decreased modelled protection trips from 3274 to 3066 events (−208; −6.35%). In contrast, accumulated time above 1.10 p.u. increased by 26.989 h (+3.25%). Therefore, the incremental benefit of the P(U) layer was concentrated in critical-overvoltage mitigation and protection-event reduction rather than in uniformly improving voltage performance.

Effective P(U) curtailment was nonzero in 113 of the 400 scenarios and totalled 6.016 MWh across the fixed scenario matrix. Despite this direct active power curtailment, generated PV energy increased by 8.781 MWh (+0.41%) relative to Fuzzy Q-only control. This net energy increase represents a closed-loop result incorporating protection trips, disconnection, reconnection, and post-reconnection active power ramping; it cannot be attributed solely to avoided protection-trip losses. Overall, these findings indicate that the selective P(U) layer primarily serves as a critical-overvoltage mitigation mechanism rather than a general voltage-quality regulator.

Seven controlled ablation experiments were performed using the same 400 matched scenario inputs. The aggregate results relative to the nominal Fuzzy Q + P controller are summarized in Table 6. Removing the one-step post-Q voltage prediction increased the accumulated duration above 1.11 p.u. by 0.336 h and produced one additional modelled

protection trip. Removing the overvoltage-warning timer increased critical-overvoltage duration by 10.436 h, whereas removing SCR/X/R-conditioned network adaptation increased it by 8.624 h but reduced the number of modelled protection trips by 27 and decreased reactive-power effort. Excluding the reactive-power-headroom input from the Fuzzy Q stage produced only minor changes in critical-overvoltage exposure and protection-trip counts. These results indicate that the individual controller components do not contribute uniformly across all performance criteria. Their effects must therefore be interpreted as multi-criteria trade-offs rather than independent improvements.

Table 6. Ablation results relative to the nominal Fuzzy Q + P controller across 400 matched scenarios.

Removed Component	ΔT > 1.11 (h)	ΔTrips	ΔQ Effort (MVArh)	ΔPV Energy (MWh)	ΔP(U) Curtailment (MWh)
No dU/dt	+0.214	−2	−41.158	−4.390	−0.086
No SCR/X/R adaptation	+8.624	−27	−36.482	+9.901	−0.632
No warning timer	+10.436	+3	−0.009	+0.253	−0.273
No Fuzzy Q headroom input	−0.054	−1	+5.381	+0.351	−0.001
No P(U) Q-saturation awareness	+4.446	+14	−0.795	−0.332	−0.769
No capability-state information	+4.362	+13	+4.580	−0.034	−0.778
No post-Q prediction	+0.336	+1	−0.276	−0.054	+0.049

Note: All differences are calculated as the ablated variant minus the nominal Fuzzy Q + P controller across the same 400 matched scenarios. Positive changes in critical-overvoltage duration and protection-trip counts indicate deterioration, whereas negative changes indicate improvement. Reactive-power effort is evaluated as the integral of absolute reactive power. P(U) curtailment represents the effective energy curtailed directly by the active power control layer and is distinct from the total reduction in generated PV energy.

The additional ablation results show that removing P(U) reactive-power saturation awareness increased critical-overvoltage exposure by 4.446 h and produced 14 additional modelled protection trips. Removing both capability-state information channels increased exposure by 4.362 h and produced 13 additional trips. By comparison, removing the one-step post-Q voltage prediction increased critical-overvoltage exposure by only 0.336 h and produced one additional trip. These results suggest that warning-state information and reactive-power capability awareness have a greater influence on the investigated performance metrics than the one-step prediction alone. However, the individual effects differ across voltage exposure, protection activity, reactive-power effort, and PV-energy utilization.

To provide a mechanism-oriented interpretation of the selective P(U) control, three representative scenarios were examined using matched Fuzzy Q and Fuzzy Q + P simulations (Figure 6). In Case 119, the proposed controller reduced critical-overvoltage exposure from 4.215 to 1.529 h and eliminated 20 modelled protection trips, with 443.036 kWh of effective P(U) curtailment. In Case 104, neither strategy produced protection trips or exposure above 1.11 p.u., although selective P(U) curtailed 2.416 kWh, indicating no additional benefit in the selected safety metrics. In Case 400, P(U) intervention did not prevent protection events: the number of modelled trips increased from 35 to 36, while critical-overvoltage exposure increased from 4.635 to 4.656 h. These scenario-level results demonstrate that the effectiveness of the selective P(U) mechanism depends on the operating conditions and cannot be generalized as uniformly beneficial.

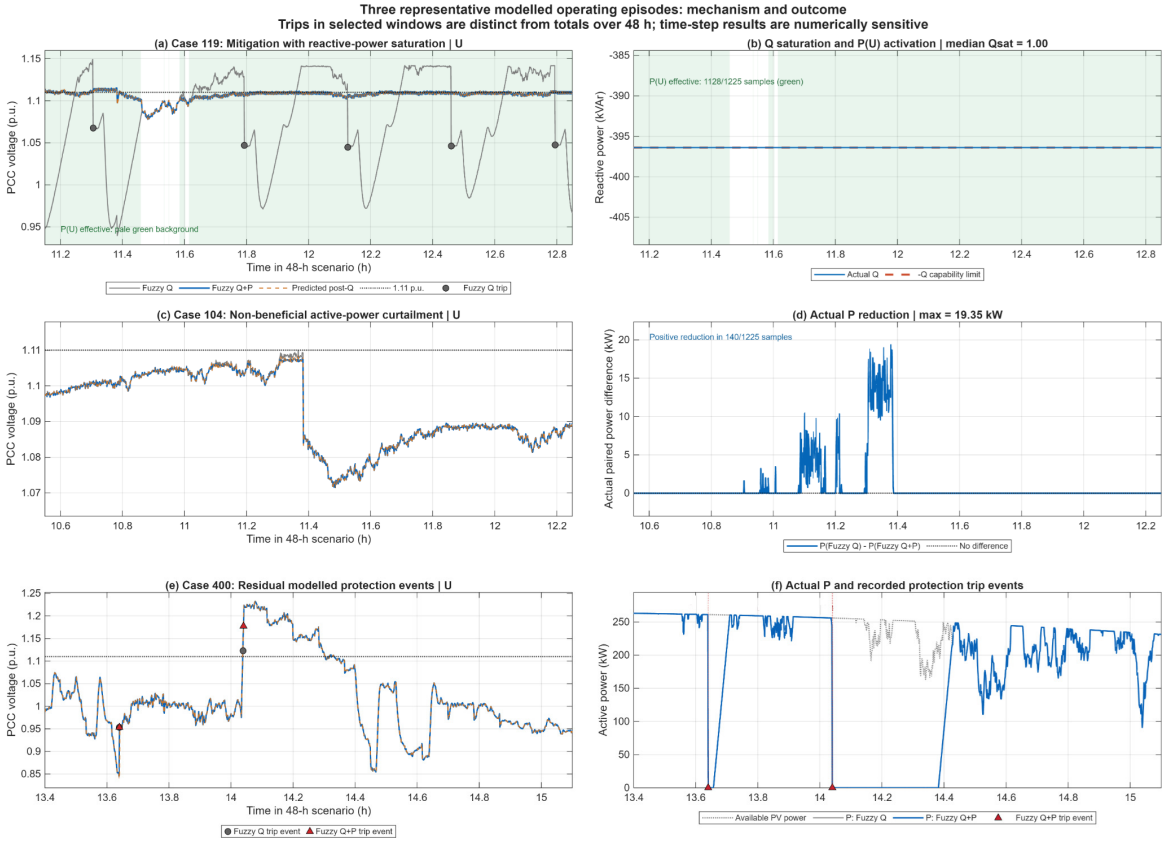


Figure 6. Mechanism-oriented comparison of the proposed Fuzzy Q + P controller and adaptive Fuzzy Q in three representative operating scenarios. (**a**,**b**) Case 119: successful mitigation of critical overvoltage through reactive-power saturation awareness and selective P(U) activation. (**c**,**d**) Case 104: active power curtailment without additional benefit in the selected voltage-security metrics. (**e**,**f**) Case 400: residual overvoltage and modelled protection events despite P(U) intervention. The displayed time windows are excerpts from 48 h simulations. Full-scenario protection-trip counts are 20 versus 0 (Case 119), 0 versus 0 (Case 104), and 35 versus 36 (Case 400), for Fuzzy Q and Fuzzy Q + P, respectively. Modelled protection-trip results remain sensitive to the simulation time step.

Figure 6 illustrates the resulting PCC voltage, active power, and protection responses, while the internal P(U) activation mechanism, including predicted post-Q voltage, reactive-power saturation, and warning-timer conditions, is described in Section 2.4 and Table 2.

The dependence of the selective P(U) mechanism on operating conditions is examined in Section 3.4.

3.4. Dependence on PV, Load, and Grid Conditions

To assess how the incremental P(U) layer depends on the scenario, the paired Fuzzy Q + P–Fuzzy Q results were organized by the available-PV profile, the load condition, the predefined paired (SCR, X/R) network conditions, and the upstream-system scenario. Since the 400 cases form a fixed factorial scenario set and SCR and X/R are linked within each predefined network equivalent, the grouped findings are best understood descriptively rather than as independent causal effects. The resulting scenario-dependent average paired reductions in critical-overvoltage exposure, $T(U_{PCC} > 1.11)$, are reported in Figure 7.

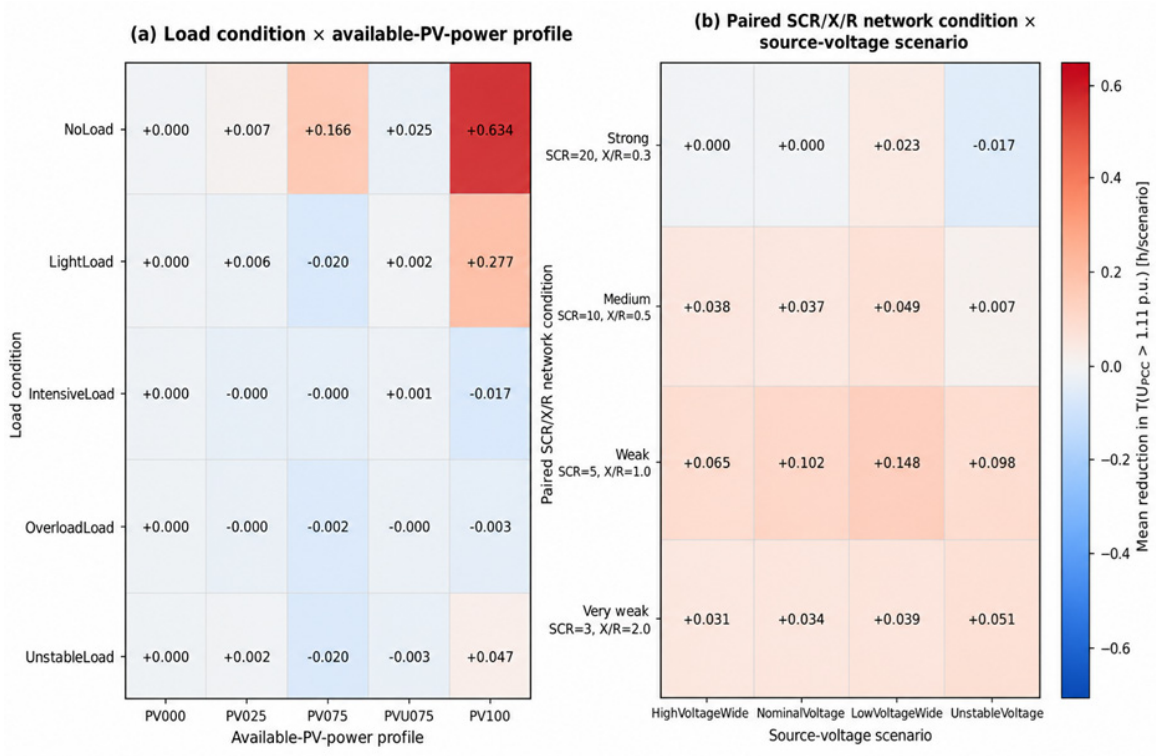


Figure 7. Scenario-dependent benefit of the selective P(U) layer in reducing critical-overvoltage exposure. (**a**) Mean paired benefit in $T(U_{PCC} > 1.11)$ across load conditions and available-PV-power profiles; (**b**) mean paired benefit across the predefined paired SCR/X/R network conditions and upstream-system scenarios. Positive values indicate a reduction in critical-overvoltage duration for Fuzzy Q + P relative to Fuzzy Q.

Positive values mean a shorter critical-overvoltage exposure with Fuzzy Q + P than with Fuzzy Q. The group means cover all matched scenarios within each category, including instances where no effective P(U) curtailment took place.

The incremental reduction in critical-overvoltage duration above 1.11 p.u. due to selective P(U) control was concentrated under high PV availability and lower load conditions. For PV100, the aggregate reduction reached 12.063 h across 80 matched scenarios, whereas PV000 showed no change. The NoLoad and LightLoad groups contributed 8.272 and 6.136 h, respectively.

Across the four predefined paired network conditions, the total reduction was 0.335 h for StrongNetwork, 6.067 h for MediumNetwork, 0.565 h for WeakNetwork, and 7.989 h for VeryWeakNetwork. These differences were not monotonic with network strength because SCR and X/R were coupled within each network case, very-weak-grid controller parameters differed from those applied under other network conditions, and protection interactions could alter the closed-loop operating trajectories. Overall, the results indicate that the effectiveness of selective P(U) control depends on the combined operating conditions rather than on network strength alone.

An additional discrete SCR–X/R sensitivity analysis (Figure A1) revealed a strong dependence of the relative controller performance on network conditions. At SCR = 3 and X/R = 0.3, the proposed Fuzzy Q + P controller reduced modelled protection trips by 38.875 events/scenario relative to conventional Q(U) + P(U) but increased critical-overvoltage duration by 1.707 h/scenario. These findings demonstrate a trade-off between voltage exposure and modelled protection activity rather than uniform superiority of the proposed controller. The supplementary 35-point SCR–X/R sensitivity analysis was restricted

to eight high-PV operating scenarios; therefore, the observed performance differences should not be generalized to the continuous SCR–X/R domain.

3.5. Repeatability, Sensitivity, and Practical Interpretation

The repeatability of the principal Fuzzy Q + P versus Q(U) trade-off was evaluated using the separately generated 400-scenario synthetic repeatability matrix defined in Section 2.6. A different random-number base seed (7300) was applied to generate new upstream-system, load, and available photovoltaic realizations, while the scenario definitions, parameter ranges, four predefined SCR–X/R network cases, and controller formulations were maintained. The main performance trends found in the original matrix were replicated for critical-overvoltage exposure, point of common coupling voltage root-mean-square error, modelled voltage-protection trips, generated photovoltaic energy, and reactive-power effort (Table 7). By contrast, the direction of change in $T(U_{PCC} > 1.10$ p.u.) was not reproduced: Fuzzy Q + P increased the exposure duration by 2.99% relative to Q(U) in the updated main scenario matrix, whereas the separately reported repeatability matrix showed a decrease of 0.634%. Accordingly, the repeatability assessment supports the persistence of the main multi-criteria trade-off rather than the invariance of every individual metric, and it is not taken as a test of statistical significance or as experimental controller validation.

Table 7. Repeatability of the principal Fuzzy Q + P versus Q(U) performance trends.

Performance Metric	Main Matrix, %	Repeatability Matrix, %	Interpretation
$T(U_{PCC} > 1.11)$	−2.20	−2.540	Favourable direction repeated
PCC voltage RMSE to V_{target}	−0.64	−0.260	Favourable direction repeated
Modelled voltage-protection trips	−3.98	−2.668	Favourable direction repeated
Generated PV energy	−0.23	−0.966	Energy penalty repeated
Reactive-power effort	+48.33	+51.727	Higher Q effort repeated
$T(U_{PCC} > 1.10)$	+2.99	−0.634	Direction not repeated

Note: Relative changes are calculated with respect to Q(U) within each 400-scenario matrix. Negative changes in voltage exposure duration, RMSE, and protection trips are favourable; for generated PV energy, a positive change is favourable, whereas lower reactive-power effort is favourable. The scenario sets are fixed comparative matrices rather than statistically independent Monte Carlo replications.

At the scenario level, Fuzzy Q + P improved critical-overvoltage duration relative to Q(U) in 66 of 400 cases (16.5%), produced no change in 303 cases (75.75%), and deteriorated it in 31 cases (7.75%). For modelled protection trips, 40 cases improved (10.0%), 321 were unchanged (80.25%), and 39 deteriorated (9.75%). The 40 scenarios with the largest positive reductions in critical-overvoltage duration accounted for 98.93% of the sum of all positive scenario-level reductions (22.229 h), rather than 98.93% of the net aggregate reduction (15.813 h), because deteriorations in other scenarios partly offset these gains. This indicates that the benefit was concentrated in a limited subset of stressed operating conditions. Accordingly, the aggregate improvement should not be interpreted as a widespread benefit across the complete scenario matrix.

To further characterize scenario-level variability relative to the reference Q(U) controller, the proposed Fuzzy Q + P controller reduced PCC voltage RMSE in 227 of the 400 scenarios (56.75%), left it unchanged in 106 (26.50%), and increased it in 67 (16.75%). Generated PV energy increased in 48 scenarios (12.00%), remained unchanged in 274 (68.50%), and decreased in 78 (19.50%). Absolute reactive-power effort decreased in 13 scenarios (3.25%), remained unchanged in 106 (26.50%), and increased in 281 (70.25%). These results indicate that improvements in voltage RMSE were more widespread than reduc-

tions in critical-overvoltage exposure, whereas increased reactive-power effort occurred in most scenarios.

Relative to conventional Q(U) + P(U), the proposed Fuzzy Q + P controller reduced critical-overvoltage duration in 50 of the 400 matched scenarios, left it unchanged in 314 scenarios, and increased it in 36 scenarios. Figure 8 presents the paired scenario-level changes relative to both reference Q(U) and conventional Q(U) + P(U). The predominance of unchanged scenarios indicates that the aggregate performance improvements reported in Table 5 are concentrated in a subset of operating conditions rather than being uniformly distributed across the scenario matrix.

The limited sensitivity assessment applied the same repeatability inputs and only varied the selected Fuzzy Q + P parameters specified in Section 2.6. Compared with the nominal controller, the later-activation P(U) threshold set lowered the effective P(U) curtailment energy by 1.166 MWh (17.67%) and increased the generated PV energy by 0.321 MWh (0.015%), yet it raised $T(U_{PCC} > 1.11)$ by 1.929 h and increased the number of modelled voltage-protection trips by 11. In contrast, the earlier-activation threshold set increased the effective P(U) curtailment energy by 1.174 MWh (17.79%) and reduced $T(U_{PCC} > 1.11)$ by 5.010 h; the total number of modelled voltage-protection trips stayed the same, and the generated PV energy fell by 0.875 MWh (0.040%). These energy changes are aggregated results across the fixed 400-case repeatability matrix and are not estimates of annual energy.

Raising the activation threshold for the VeryWeakGuard SCR from 3.0 to 3.5 did not affect the assessed metrics. This outcome is consistent with the discrete network set employed in the study, which includes only SCR values of 20, 10, 5, and 3. In particular, the case of SCR = 3 with X/R = 2.0 already triggers the very-weak-grid parametrization under the nominal setting, and there are no scenarios in the interval $3 < \text{SCR} \leq 3.5$. Therefore, the observed zero change does not indicate a general insensitivity to SCR; rather, it shows that this threshold perturbation leaves the controller mode assigned to every scenario in the implemented matrix unchanged.

The supplementary OAT sensitivity analysis identified the P(U) activation-voltage threshold as the most influential parameter group among those investigated. Across its five tested levels, the cumulative duration above 1.11 p.u. varied by 22.083 h, modelled protection trips by 100 events, and effective P(U)-curtailed energy by 3.201 MWh over the 12 selected scenarios. Relative to the nominal setting, earlier P(U) activation reduced critical-overvoltage duration by 8.347 h and protection trips by 33 events, while increasing direct P(U) curtailment by 1.592 MWh. These results demonstrate the substantial influence of the activation threshold on the voltage-security–curtailment trade-off.

Network-adaptation gains produced the largest variation in absolute reactive-power effort (5.404 MVArh), while their influence on critical-overvoltage duration (0.301 h) and protection trips (two events) was considerably smaller. Several other investigated parameter groups produced limited or no observable changes under the selected conditions. These findings indicate that parameter influence differs across performance criteria. However, the analysis covers only 12 selected high-PV scenarios and does not establish global controller robustness; protection-trip comparisons also remain subject to the numerical time-step limitations discussed above.

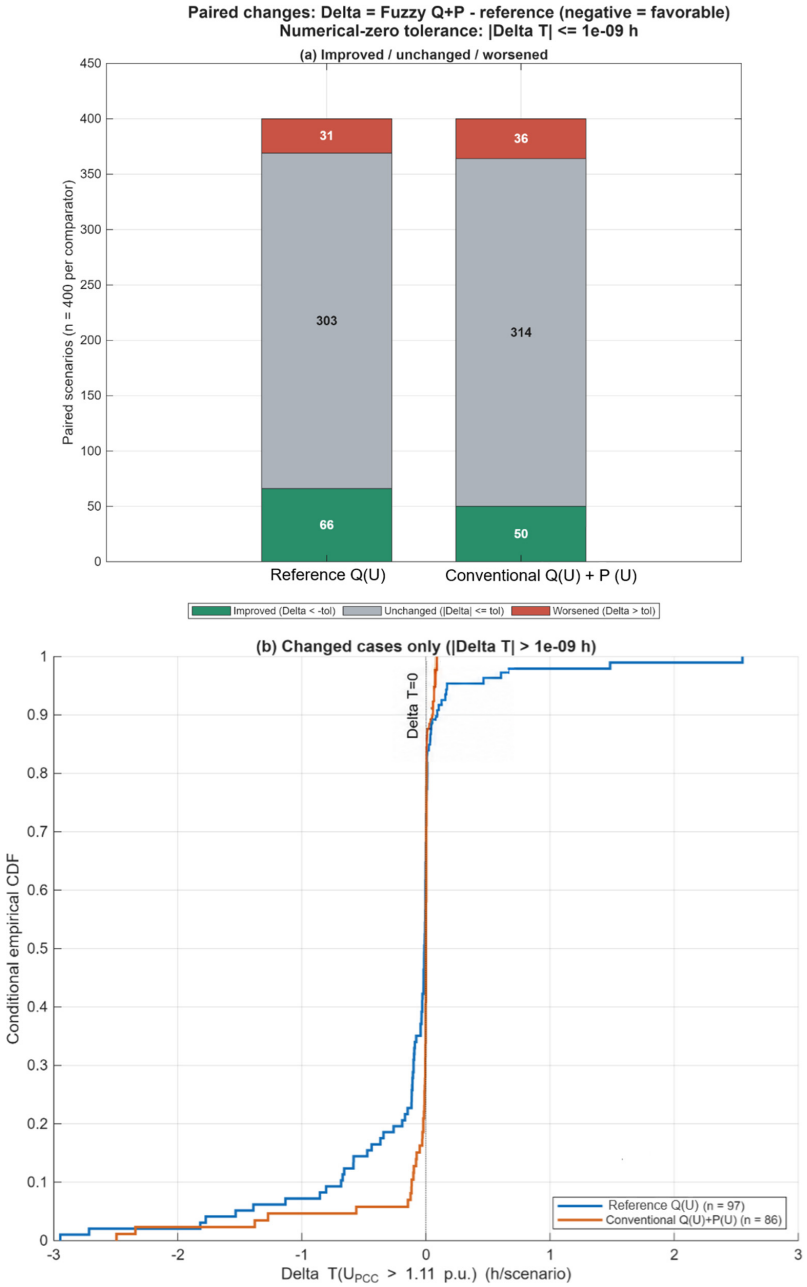


Figure 8. Scenario-level paired changes in critical-overvoltage duration for the proposed Fuzzy Q + P controller relative to reference Q(U) and conventional Q(U) + P(U) across 400 matched 48 h scenarios. (**a**) Numbers of scenarios with improved, unchanged, or worsened performance. (**b**) Conditional empirical cumulative distributions of nonzero paired differences for reference Q(U) (n = 97) and conventional Q(U) + P(U) (n = 86). Differences are calculated as Fuzzy Q + P minus the corresponding comparator; negative values indicate favourable changes. Differences with absolute magnitudes not exceeding 10^{-9} h are classified as unchanged.

To further examine the voltage-security–curtailment trade-off associated with P(U) parameter selection, 25 controller settings were evaluated using the same 12 selected operating scenarios (Figure 9). The results show that greater effective active power curtailment was generally associated with shorter critical-overvoltage exposure and fewer modelled protection events. The nominal controller setting represents one operating compromise rather than a demonstrated optimum. Since this analysis covers only 12 selected scenarios, its results should not be generalized to the complete 400-scenario matrix.

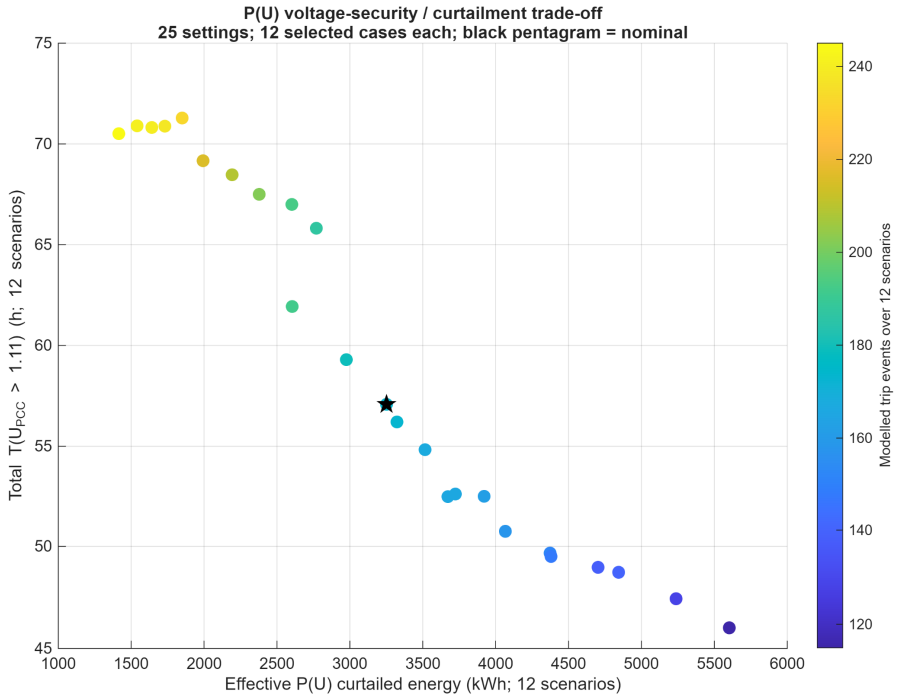


Figure 9. Voltage security and active power curtailment trade-off for 25 P(U) controller settings evaluated across 12 selected matched 48 h scenarios. Each point represents the cumulative effective P(U)-curtailed energy (kWh) and critical-overvoltage duration above 1.11 p.u. (h) across the 12 scenarios. The colour indicates the total number of modelled protection-trip events, while the black star denotes the nominal controller setting. The analysis illustrates a local parameter-dependent trade-off rather than global parameter optimality. Modelled protection-trip counts remain sensitive to the simulation time step.

Taken as a whole, the findings support a simulation-based operational interpretation of Fuzzy Q + P as an adjustable and selective approach for mitigating residual overvoltage within the investigated scenario set. Specifically, when the P(U) layer is activated earlier, the resulting operating compromise shifts toward reduced exposure to high voltage, but this benefit is accompanied by a stronger need to curtail active power. By contrast, when activation occurs later, the degree of active power curtailment can be reduced, while the system correspondingly permits a greater level of high-voltage exposure. Accordingly, the repeatability and sensitivity assessments reinforce the scenario-based interpretation of the trade-off that is observed across conditions. However, these checks are not sufficient to demonstrate global controller robustness, to prove that the chosen parameters are optimal, or to establish that performance is insensitive throughout a continuous range of SCR–X/R values.

The time-step convergence assessment did not meet the predefined numerical acceptance criteria (Figure 10). Of the 67 evaluated comparisons, 15 were classified as PASS, 49 as NUMERICALLY_SENSITIVE, and 3 as INCONCLUSIVE; an additional 24 finest-step results served as numerical references. Moreover, 24 changes in the direction of paired performance differences were identified. The representative Cases 14, 19, and 319 illustrate that both critical-overvoltage exposure and modelled protection-trip counts may depend on the simulation time step. Consequently, protection-related comparisons at the nominal 5 s resolution cannot be considered time-step-invariant or experimentally validated. Further event-level investigation and finer-resolution simulations are required before numerical convergence and reliable protection-performance improvements can be claimed.

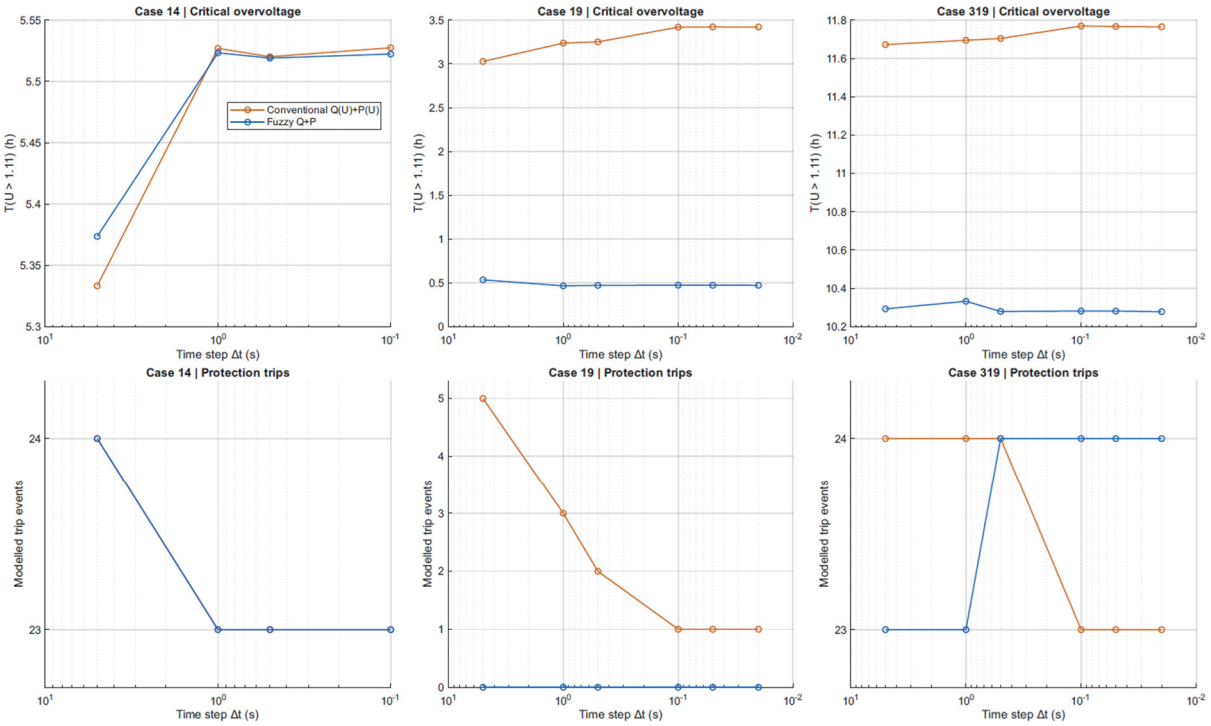


Figure 10. Numerical time-step sensitivity of conventional Q(U) + P(U) and the proposed Fuzzy Q + P controllers for three selected operating scenarios (Cases 14, 19, and 319). The upper panels show accumulated critical-overvoltage duration above 1.11 p.u., while the lower panels present the corresponding modelled protection-trip counts at different simulation time steps. The predefined numerical convergence acceptance criteria were not satisfied. The results illustrate the sensitivity of selected voltage performance and protection-event indicators to temporal discretization.

In Case 14, the protection-trip curves of conventional Q(U) + P(U) and Fuzzy Q + P overlap completely, as both controllers produce identical trip counts at all evaluated time steps (24 events at $\Delta t = 5$ s and 23 events at $\Delta t \leq 1$ s).

3.6. Scientific Contribution and Limitations

The scientific contribution lies in the causal integration of state- and network-conditioned Fuzzy Q control, one-step post-Q voltage assessment, and selective P(U) activation within a reactive-power-priority architecture, rather than in the individual application of established control techniques. Here, "adaptive" refers to controller responses conditioned on the operating state and predefined SCR/X/R network conditions, not online network-parameter identification. An internal Q(U)-based safety constraint prevents insufficient reactive-power absorption at elevated voltages, while the predicted post-Q voltage informs selective P(U) activation, as detailed in Sections 2.3 and 2.4.

A further contribution lies in the matched multi-criteria assessment of this architecture across a fixed 400-scenario factorial matrix, along with a direct Fuzzy Q versus Fuzzy Q + P comparison designed to isolate the incremental effect of the P(U) layer. The findings show a scenario-dependent operational trade-off rather than consistent superiority over the reference Q(U) controller: reductions in critical-overvoltage exposure and modelled protection activity are achieved at the expense of higher reactive-power utilization and a small active-energy penalty relative to Q(U). The independent repeatability matrix and restricted parameter perturbations indicate that the main trade-off persists, but they should not be taken as evidence of global robustness or parameter optimality. This reading aligns with the earlier results, in which the dominant performance trends were reproduced even though every individual metric did not remain invariant.

Relative to fixed Q(U), Fuzzy Q + P required an additional 0.741 MVArh of absolute reactive-power effort per scenario, while reducing critical-overvoltage duration by 0.0395 h (2.37 min) and modelled protection events by 0.318 per scenario. Across the full 400-case aggregate, this corresponds descriptively to approximately 3.20 min of reduced $T(U_{PCC} > 1.11$ p.u.) and 0.429 fewer modelled trip events per additional MVArh. These are aggregate closed-loop ratios, not physical marginal dU/dQ sensitivities or the isolated causal benefit of reactive-power absorption, because Fuzzy Q + P also applies selective active power curtailment. The effectiveness and dynamic behaviour of Volt–Var control depend on control-curve settings, response time, network voltage sensitivity, and system strength, while overly aggressive settings may reduce stability margins. Consequently, the additional reactive-power absorption observed in the proposed controller should be interpreted in relation to the voltage-security and protection benefit that it produces, rather than as an independent indication of improved controller performance [3].

In the reactive-power-only comparison, Fuzzy Q required 0.728 MVArh more absolute reactive-power effort per scenario than fixed Q(U), while reducing exposure above 1.11 p.u. by only 0.00214 h (0.129 min) per scenario; modelled trips increased by 0.203 events per scenario. Thus, the additional Q effort of the adaptive Fuzzy Q stage alone did not yield a consistent protection benefit in the tested scenarios. This distinction prevents attribution of the combined Fuzzy Q + P outcome solely to adaptive reactive-power control.

The primary comparison used a single fixed Q(U) setting. Although five representative Q(U) characteristics were evaluated in the supplementary sensitivity analysis (Table A1), neither an optimized nor scenario-specific Q(U) tuning was performed; thus, the findings cannot be generalized to all conventional Q(U) parameterizations. A direct conventional Q(U) + P(U) benchmark and a Q(U) + shared-P(U) ablation benchmark were included in the updated study. Their results indicate that part of the critical-overvoltage mitigation can be achieved through combined Volt–Var/Volt–Watt operation without the adaptive Fuzzy Q stage. In the investigated scenario set, Fuzzy Q + P achieved a modest reduction in critical-overvoltage duration relative to conventional Q(U) + P(U), but resulted in more modelled protection events, greater reactive-power effort, and lower generated PV energy. The ablation analysis (Table 6) showed that removing the one-step post-Q voltage prediction increased critical-overvoltage duration by only 0.336 h across 400 scenarios and resulted in one additional modelled protection trip, indicating its limited independent numerical contribution. The study therefore demonstrates a particular controller architecture and a quantified scenario-dependent operating trade-off, rather than a general performance advantage over conventional or optimized combined-control strategies. The study employs a balanced three-phase quasi-steady-state equivalent to an aggregated PV inverter and four predefined paired SCR and X/R network conditions; it does not replicate a detailed unbalanced multi-node low-voltage feeder, phase asymmetry, neutral-conductor behaviour, or interactions among multiple independently controlled inverters. Transformer thermal limits, thermal ageing, and allowable overload duration were not modelled; consequently, the high-load, overload, and highest-PV/low-load combinations are used as voltage-control stress cases and should not be interpreted as representing permissible continuous transformer operating conditions. The nominal 5 s simulation step does not resolve sub-second protection dynamics. Furthermore, the separate time-step convergence assessment did not meet its predefined acceptance criteria. Consequently, modelled protection-trip counts, and protection-dependent energy outcomes may be affected by temporal discretization. These results must therefore be interpreted as comparative numerical indicators within the implemented sampled-data model, rather than as time-step-invariant estimates, experimentally demonstrated protection improvements, or evidence of compliance with grid-code protection requirements. In addition, the 400 scenarios form a fixed comparative factorial set

rather than statistically independent Monte Carlo realizations, and the aggregated energy quantities therefore do not correspond to annual energy yield.

A further consideration for future extension of the proposed voltage-control framework concerns its application to PV–battery energy-storage systems. In such applications, electrical P–Q capability should not be considered independently of battery-safety constraints. Lithium-ion thermal runaway can be initiated by internal short circuits, overcharging, or excessive thermal exposure and may lead to rapid temperature rise, flammable-gas release, fire, and propagation to adjacent cells [28]. Recent experimental studies have shown that thermal management and insulating materials can delay thermal-runaway onset and mitigate propagation between cells [8]. The severity of thermal-runaway events is also strongly influenced by state of charge and installation confinement, which affect combustion intensity, heat transfer, and propagation risk [29]. Therefore, future PV–BESS extensions of the proposed controller should incorporate battery management and thermal management constraints rather than treating the storage system solely as an additional active- and reactive-power actuator.

Finally, the real-site measurements confirm only the equivalent LV feeder-voltage calculation within the observed voltage range, and they do not experimentally validate the Q(U), Fuzzy Q, Fuzzy Q + P, P(U), or protection functions. Controller sensitivity was assessed through selected P(U) activation and network-adaptation threshold perturbations, as well as an additional bounded one-at-a-time analysis of 10 parameter groups across 12 selected high-PV scenarios. These analyses do not establish global parameter robustness. Consequently, practical deployment would require site-specific parameterization and additional validation in detailed unbalanced networks under experimental or hardware-in-the-loop conditions, including measurement uncertainty, implementation delays, multi-inverter interactions, and coordination with other voltage-regulation devices.

Power hardware-in-the-loop (PHIL) and controller hardware-in-the-loop (CHIL) approaches provide a relevant next validation stage beyond offline simulation because they enable smart-inverter functions to be evaluated under controlled real-time grid conditions. Recent PHIL implementations have demonstrated the testing of commercial smart inverters operating with Volt–Var and Volt–Watt functions and integrated with DERMS environments, providing a suitable experimental framework for future validation of the proposed controller [30].

4. Conclusions

1. A reactive-power-priority adaptive Fuzzy Q + P controller was implemented and compared with an uncontrolled baseline, fixed Q(U), conventional Q(U) + P(U), Q(U) + shared-P(U), and adaptive Fuzzy Q under 400 matched 48 h scenarios. The proposed approach integrates network-conditioned Fuzzy Q, one-step post-Q voltage assessment, and selective active power curtailment under common inverter and protection constraints.
2. Relative to Q(U), the proposed controller decreased exposure above 1.11 p.u. by 2.20% and modelled protection trips by 3.98%, while increasing reactive-power effort by 48.33% and decreasing generated PV energy by 0.23%. Compared with conventional Q(U) + P(U), exposure above 1.11 p.u. was 1.17% lower, but modelled trips were 1.59% higher, reactive-power effort was 46.89% higher, and PV generation was 0.57% lower. Therefore, the performance advantage is criterion- and scenario-dependent.
3. The selective P(U) layer reduced $T(U_{PCC} > 1.11$ p.u.) by 2.08% and modelled trip events by 6.35% relative to Fuzzy Q-only control. Effective curtailment occurred in 113 scenarios and totalled 6.016 MWh over the fixed scenario matrix. The associated

net energy change reflects the full protection and reconnection trajectory rather than active power curtailment alone.

4. Scenario-level and ablation analyses indicated that benefits were concentrated in a relatively small subset of critical operating conditions. The post-Q prediction produced only a limited independent numerical contribution within the examined conditions, and the shared-P(U) comparison did not establish a universal benefit from the adaptive Fuzzy Q stage.
5. Validation against 81,951 real-site samples supported only the equivalent LV feeder-voltage calculation (RMSE = 0.001038 p.u.). The investigated control algorithms and protection functions were not experimentally validated. Numerical time-step convergence was not demonstrated, with 49 of 67 evaluated comparisons classified as NUMERICALLY_SENSITIVE. Therefore, protection-related differences should be interpreted as comparative indicators within the sampled 5 s model, rather than as time-step-independent or experimentally confirmed improvements. Hardware-in-the-loop validation and evaluation using an unbalanced multi-node, multi-inverter network model remain necessary to establish broader practical applicability.

Author Contributions: Conceptualization, D.S. and V.R.; methodology, D.S.; software, D.S.; validation, D.S.; formal analysis, D.S.; investigation, D.S.; data curation, D.S.; writing—original draft preparation, D.S.; writing—review and editing, D.S.; visualization, D.S.; supervision, D.S.; project administration, D.S. All authors have read and agreed to the published version of the manuscript.

Funding: This research received no external funding.

Data Availability Statement: The aggregated results supporting the findings of this study are reported in the article. The MATLAB controller definitions required to verify and reproduce the implemented Q(U), Fuzzy Q, and Fuzzy Q + P control logic, including the Fuzzy rule base, membership-function parameters, controller scaling factors, and P(U) activation logic, are available from the corresponding author upon reasonable request and may also be provided for peer-review verification where appropriate. The complete scenario libraries, raw research datasets, and full MATLAB project are not publicly deposited because they form part of ongoing doctoral research.

Acknowledgments: We sincerely thank the reviewers for their insightful constructive criticism and invaluable suggestions, which greatly improved this paper.

Conflicts of Interest: The authors declare no conflicts of interest.

Abbreviations

The following abbreviations are used in this manuscript:

AC	Alternating current
CT/VT	Current transformer/voltage transformer
FLC	Fuzzy logic controller
LV	Low voltage
MAE	Mean absolute error
OLTC	On-load tap changer
PCC	Point of common coupling
PV	Photovoltaic
RMSE	Root-mean-square error
SCR	Short-circuit ratio
p.u.	Per unit

Appendix A

Table A1. Sensitivity of fixed Q(U) and conventional Q(U) + P(U) controllers to slope and deadband variations across 400 matched 48 h scenarios.

Q(U) Setting	Curve [UA, UB, UC, UD] (p.u.)	Controller	T > 1.11 (h/Scenario)	Trips (Events/Scenario)	|Q| (MVArh/Scenario)	PV Energy (MWh/Scenario)
Slope/steeper	(0.92, 0.95, 1.05, 1.08)	Q(U)	1.798878	7.9625	1.6597	5.4438
Slope/steeper	(0.92, 0.95, 1.05, 1.08)	Conventional Q(U) + P(U)	1.781000	7.5125	1.6747	5.4634
Slope/standard	(0.91, 0.95, 1.05, 1.09)	Q(U)	1.800698	7.9825	1.5326	5.4429
Slope/standard	(0.91, 0.95, 1.05, 1.09)	Conventional Q(U) + P(U)	1.782066	7.5450	1.5476	5.4614
Slope/flatter	(0.89, 0.95, 1.05, 1.11)	Q(U)	1.822677	8.0200	1.3183	5.4356
Slope/flatter	(0.89, 0.95, 1.05, 1.11)	Conventional Q(U) + P(U)	1.796833	7.5775	1.3331	5.4528
Deadband/narrow	(0.92, 0.96, 1.04, 1.08)	Q(U)	1.798736	7.9425	1.8742	5.4473
Deadband/narrow	(0.92, 0.96, 1.04, 1.08)	Conventional Q(U) + P(U)	1.781253	7.4975	1.8882	5.4661
Deadband/wide	(0.90, 0.94, 1.06, 1.10)	Q(U)	1.804198	8.0150	1.2304	5.4359
Deadband/wide	(0.90, 0.94, 1.06, 1.10)	Conventional Q(U) + P(U)	1.784052	7.5750	1.2466	5.4545
Fuzzy Q + P (unchanged)	Not a Q(U) curve	Proposed Fuzzy Q + P	1.761167	7.6650	2.2733	5.4301

Note. Five distinct Q(U) characteristics were evaluated for two fixed-curve controllers using the same 400 matched 48 h scenarios per variant. The four voltage values (UA, UB, UC, UD) define the Q(U) characteristic breakpoints. The corresponding normalized reactive-power values at these breakpoints are (+0.484, 0, 0, −0.484) for all five characteristics. The proposed Fuzzy Q + P controller was evaluated without parameter modifications and serves as a common reference. All reported metrics are means per scenario. The duration above 1.11 p.u. represents voltage exposure and must not be equated with protection-trip counts. Modelled protection-trip results remain sensitive to the simulation time step. This analysis assesses the five selected Q(U) characteristics and does not establish superiority over globally optimized Q(U) settings.

Table A2. Bounded one-at-a-time sensitivity of Fuzzy Q + P controller parameters across 12 selected high-PV scenarios.

Parameter Group	Tested Range	T > 1.11 Range (h)	Trips Range	Q Effort Range (kVArh)
P(U) activation voltage	1.095–1.115 p.u. *	22.083	100	2506.4
Network-adaptation gains	±25%	0.301	2	5403.7
P(U) ramp-down rate	0.075–0.125 P_n/min	1.253	2	19.2
Voltage-derivative filter	±25%	0.246	0	271.3
Q tracking time constant 1	11.25–18.75 s	0.160	3	358.7
Q tracking time constant 2	22.5–37.5 s	0.163	2	325.4
Safety-voltage thresholds	±0.01 p.u.	0.007	0	462.3
Warning-timer thresholds	±25%	0.010	0	0.6
High/medium fuzzy membership	1.095–1.115 p.u.	0.000	0	0.0
Q-saturation threshold	0.75–0.95	0.000	0	0.0

Note. * P(U) activation-voltage range refers to the normal-grid setting; the very-weak-grid range was 1.090–1.110 p.u. Network adaptation, safety-voltage and warning-timer groups contain jointly varied parameters. All reported ranges are maximum minus minimum across the five tested levels, aggregated over the same 12 scenarios. Protection-trip counts are subject to 5 s time-step sensitivity.

Appendix B

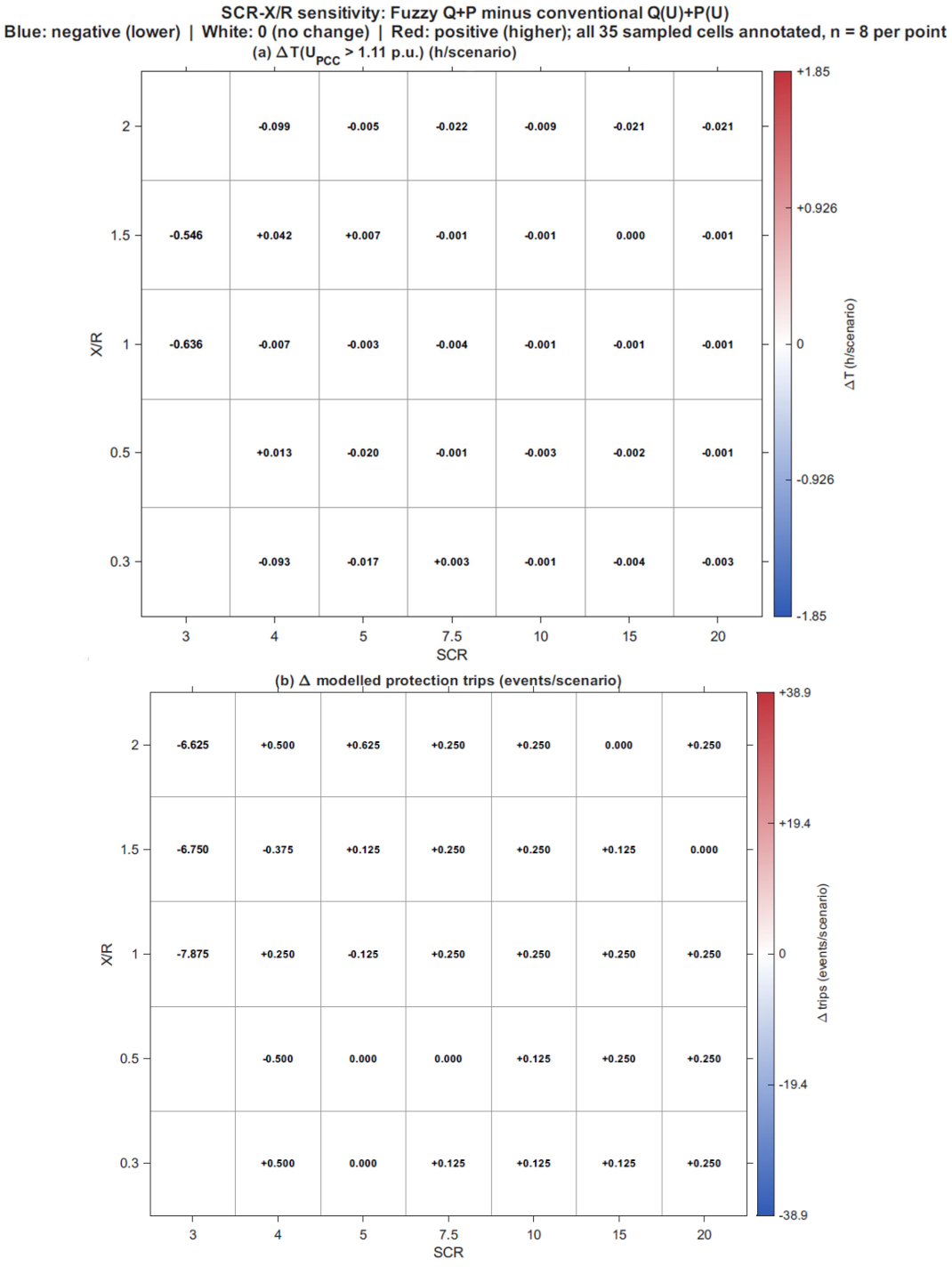


Figure A1. Discrete SCR–X/R sensitivity of the proposed Fuzzy Q + P controller relative to conventional Q(U) + P(U). (**a**) Difference in critical-overvoltage duration above 1.11 p.u. (h/scenario). (**b**) Difference in modelled protection-trip counts (events/scenario). Results cover 35 discrete SCR–X/R combinations with eight matched operating scenarios per combination. Negative values indicate lower values for the proposed controller. Protection-trip results remain sensitive to the simulation time step.

References

1. Jamil, E.; Hameed, S.; Jamil, B.; Qurratulain. Power quality improvement of distribution system with photovoltaic and permanent magnet synchronous generator based renewable energy farm using static synchronous compensator. *Sustain. Energy Technol. Assess.* **2019**, *35*, 98–116. [CrossRef]
2. Ramon-Marin, M.; Sumper, A.; Villafáfila-Robles, R.; Bergas-Jané, J. Active power estimation of photovoltaic generators for distribution network planning based on correlation models. *Energy* **2014**, *64*, 758–770. [CrossRef]
3. Zdraveski, V.; Todorovski, M.; Kocarev, L. Dynamic intelligent load balancing in power distribution networks. *Int. J. Electr. Power Energy Syst.* **2015**, *73*, 157–162. [CrossRef]
4. Zimann, F.J.; Batschauer, A.L.; Mezaroba, M.; Neves, F.A.S. Energy storage system control algorithm for voltage regulation with active and reactive power injection in low-voltage distribution network. *Electr. Power Syst. Res.* **2019**, *174*, 105825. [CrossRef]
5. Adewuyi, O.B.; Shigenobu, R.; Ooya, K.; Senjyu, T.; Howlader, A.M. Static voltage stability improvement with battery energy storage considering optimal control of active and reactive power injection. *Electr. Power Syst. Res.* **2019**, *172*, 303–312. [CrossRef]
6. Chang, H.; Vanfretti, L. Power Hardware-in-the-Loop Smart Inverter Testing with Distributed Energy Resource Management Systems. *Electronics* **2024**, *13*, 1866. [CrossRef]
7. Abo Alwez, M.; Jasni, J.; Mohd Radzi, M.A.; Azis, N. Adaptive reactive power control for voltage rise mitigation on distribution network with high photovoltaic penetration. *Renew. Sustain. Energy Rev.* **2025**, *207*, 114948. [CrossRef]
8. Khan, B.; Hayat Ullah, S.H.; Lai, C.; Mohamed, A.A.; Eicker, U. Low voltage distribution grids optimization with increasing distributed energy generation: A review. *Energy Rep.* **2026**, *15*, 108913. [CrossRef]
9. Smith, E.J.; Robinson, D.A.; Elphick, S. DER Control and Management Strategies for Distribution Networks: A Review of Current Practices and Future Directions. *Energies* **2024**, *17*, 2636. [CrossRef]
10. Almeida, D.; Pasupuleti, J.; Ekanayake, J. Comparison of reactive power control techniques for solar PV inverters to mitigate voltage rise in low-voltage grids. *Electronics* **2021**, *10*, 1569. [CrossRef]
11. Zainuddin, M.; Surusa, F.E.P.; Asri, M.; Mokoagow, A. Reactive power control of solar photovoltaic inverters for grid code compliance support. *Int. J. Appl. Power Eng.* **2023**, *12*, 300–311. [CrossRef]
12. Gupta, S.; Kekatos, V.; Chatzivasileiadis, S. Optimal Design of Volt/VAR Control Rules of Inverters Using Deep Learning. *IEEE Trans. Smart Grid* **2024**, *15*, 4731–4743. [CrossRef]
13. Abdelkader, S.M.; Kinga, S.; Ebinyu, E.; Amissah, J.; Mugerwa, G.; Taha, I.B.M.; Mansour, D.-E.A. Advancements in data-driven voltage control in active distribution networks: A comprehensive review. *Results Eng.* **2024**, *23*, 102741. [CrossRef]
14. Wang, W.; Ren, W.; Huque, A.; Van Zandt, D.; Walling, R.; Vaz, J.; Arafa, S.; Kankanamalage, R.; Walsh, N. Stability Analysis and Setting Guideline for Inverter-Based Distributed Energy Resources with Volt-Var and Volt-Watt Control Functions. In Proceedings of the 2023 IEEE Power & Energy Society General Meeting (PESGM), Orlando, FL, USA, 16–20 July 2023; pp. 1–5.
15. Parise, G.; Martirano, L.; Kermani, M.; Kermani, M. Designing a power control strategy in a microgrid using PID/fuzzy controller based on battery energy storage. In Proceedings of the 2017 IEEE International Conference on Environment and Electrical Engineering and 2017 IEEE Industrial and Commercial Power Systems Europe (EEEIC/I&CPS Europe), Milan, Italy, 6–9 June 2017; pp. 1–5.
16. Bakhoda, O.Z.; Menhaj, M.B.; Gharehpetian, G.B. MPPT for a three-phase grid-connected PV system (Fuzzy Logic Controller vs. PI Controller). In Proceedings of the 2015 4th Iranian Joint Congress on Fuzzy and Intelligent Systems (CFIS), Zahedan, Iran, 9–11 September 2015; pp. 1–5.
17. Stanelytė, D.; Narščius, A. Methodology for Mamdani Fuzzy and PID Volt–Var Control in Renewable Low-Voltage Distribution Grids: A MATLAB-Based Approach. *World* **2026**, *7*, 26. [CrossRef]
18. Hagh, M.T.; Shaker, A.; Sohrabi, F.; Gunsel, I.S. Fuzzy-based controller for DVR in the presence of DG. *Procedia Comput. Sci.* **2017**, *120*, 684–690. [CrossRef]
19. Chandrasekaran, S.; Durairaj, S.; Padmavathi, S. A performance evaluation of a fuzzy logic controller-based photovoltaic-fed multi-level inverter for a three-phase induction motor. *J. Frankl. Inst.* **2021**, *358*, 7394–7412. [CrossRef]
20. Satyam, P.; Yu, W.; Li, X. Bidirectional active control of structures with type-2 fuzzy PD and PID. *Int. J. Syst. Sci.* **2018**, *49*, 766–782. [CrossRef]
21. Letting, L.; Munda, J.; Hamam, Y. Optimization of a fuzzy logic controller for PV grid inverter control using S-function based PSO. *Sol. Energy* **2012**, *86*, 1689–1700. [CrossRef]
22. Rahman, M.; Sarker, S.; Sarkar, S.K.; Das, S.K. PHEV participating in load frequency regulation of interconnected smart grid using integral linear quadratic Gaussian control approach. In Proceedings of the 2019 International Conference on Energy and Power Engineering (ICEPE), Dhaka, Bangladesh, 14–16 March 2019; pp. 1–6.
23. Khan, I.; Li, Z.; Xu, Y.; Gu, W. Distributed control algorithm for optimal reactive power control in power grids. *Int. J. Electr. Power Energy Syst.* **2016**, *83*, 505–513. [CrossRef]

24. Gubert, T.C.; Colet, A.; Casals, L.C.; Corchero, C.; Domínguez-García, J.L.; Alvarez de Sotomayor, A.; Martin, W.; Stauffer, Y.; Alet, P.-J. Adaptive Volt–Var Control Algorithm to Grid Strength and PV Inverter Characteristics. *Sustainability* **2021**, *13*, 4459. [CrossRef]
25. Ozdemir, H.; Turkoglu, A.S.; Erdinc, O.; Pisica, I. Distributed reactive power control with adaptive Volt/VAr in active distribution systems. *IEEE Access* **2026**, *14*, 69127–69142. [CrossRef]
26. Chathurangi, D.; Jayatunga, U.; Perera, S.; Agalgaonkar, A.P.; Siyambalapitiya, T. Comparative evaluation of solar PV hosting capacity enhancement using Volt-VAr and Volt-Watt control strategies. *Renew. Energy* **2021**, *177*, 1063–1075. [CrossRef]
27. Balogun, O.A.; Sun, Y.; Gbadega, P.A. Optimal PV active power curtailment in a PV-penetrated distribution network using optimal smart inverter Volt-Watt control settings. *Energy Rep.* **2024**, *12*, 5396–5419. [CrossRef]
28. Zhang, L.; Sidhu, T.S. New dynamic voltage, and reactive power control method for distribution networks with DG integration. In Proceedings of the 2014 IEEE Electrical Power and Energy Conference (EPEC), Calgary, AB, Canada, 12–14 November 2014; pp. 190–195.
29. Franco, J.F.; Rider, M.J.; Lavorato, M.; Romero, R. A mixed-integer LP model for the optimal allocation of voltage regulators and capacitors in radial distribution systems. *Int. J. Electr. Power Energy Syst.* **2013**, *48*, 123–130. [CrossRef]
30. Nair, D.S.; Rajeev, T. Impact of reverse power flow due to high solar PV penetration on distribution protection system. In *Sustainable Energy and Technological Advancements*; Panda, G., Naayagi, R.T., Mishra, S., Eds.; Springer: Singapore, 2022; pp. 1–13.

Disclaimer/Publisher's Note: The statements, opinions and data contained in all publications are solely those of the individual author(s) and contributor(s) and not of MDPI and/or the editor(s). MDPI and/or the editor(s) disclaim responsibility for any injury to people or property resulting from any ideas, methods, instructions or products referred to in the content.